Magnetocaloric effect in layered metal hydroxides

Abstract

This research investigates the synthesis, morphology and magnetic properties of monometallic layered double hydroxides containing manganese, iron, and cobalt. In particular, the main focus was looking for layered ferromagnetic materials with high magnetic entropy change for hydrogen liquefaction while offering a more sustainable alternative to rare-earth based materials. The following compounds were characterized by X-Ray diffraction and magnetometry.

Adapting a previously discovered procedure in the group, a mixture of two phases of air sensitive manganese based layered double hydroxides was synthesised via solvent evaporation from manganese sulfate and sodium hydroxide in water. Both compositions exhibit antiferromagnetic ordering with strength of interactions being comparable along with having transitions temperatures within operational ranges for hydrogen liquefaction

Green Rust, a monometallic multivalent iron layered double hydroxide, was obtained via solvothermal treatment from iron chloride hexahydrate and sodium acetate in glycerol. Intercalation of lactate anions and thorough washing with ethanol and water proved to be integral to producing an air stable layered system. While lactate anions improved the stability of metal centers to oxidation in air, the in-plane ordering is antiferromagnetic based on Curie-Weiss fitting.

Implementation of lactate anion for air stability proved effective in synthesis of an iron based layered simple hydroxide from iron sulfate heptahydrate and sodium hydroxide in glycerol. The solvothermal treatment and subsequent washing with ethanol yielded an air stable dark green powder exhibiting antiferromagnetic ordering below 45 K. The magnetic entropy change was calculated to be 1.19 J / kg·K at 7 K at 5 Tesla.

Attempting to synthesize ferromagnetic $Co_5(OH)_6(SeO_4)_2$ 4 H_2O was not successful as the desired structure could not be obtained. A layered material was synthesised in which the majority of cobalt cations exist in their 2+ oxidation state, with the overall ratio of Co^{2+} to Co^{3+} being 11.5:1. The magnetic interactions in the material are dominated by superexchange leading to an antiferromagnetic transition at 20 K with a weak ferromagnetic component and a saturation magnetisation of 0.6 μ_B per Co atom.

Lastly, a non layered compound was obtained as crystals during investigation of manganese based layered double hydroxides which prompted further study of the material. The crystals of $Na_2MnSO_4 \cdot 2\ H_2O$ were obtained by solvent evaporation of water, and subsequent washing and recrystallizing with ~1% sulfuric acid in air. The product was obtained as black crystals exhibiting weak antiferromagnetic behaviour as suggested by the Weiss temperature of -12 K. However, measurements of the magnetisation versus temperature and field indicated that this compound remains paramagnetic down to 5 K, implying that $Na_2MnSO_4 \cdot 2\ H_2O$ crystals have low magnetic entropy changes with applied field in the hydrogen liquefaction temperature range.

1. Introduction

1.1 Magnetic refrigeration

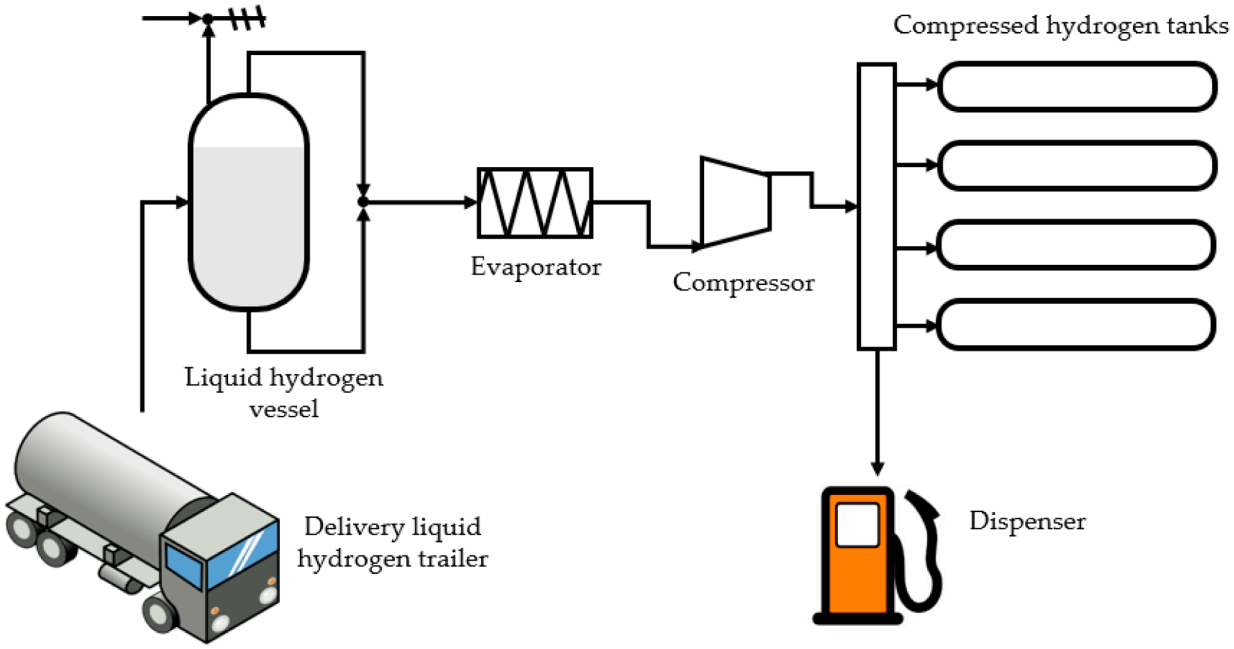

Figure 1: Hydrogen liquefaction, general scheme[1]

Magnetic refrigeration is an emerging solid-state cooling technology that operates on thermodynamic cycles involving magnetic entropy changes, offering a more sustainable and energy-efficient alternative to conventional vapor-compression refrigeration, which relies on the expansion and compression of environmentally harmful gases.[1] At cryogenic temperatures, magnetic refrigeration can outperform traditional cooling methods, especially in critical applications such as hydrogen liquefaction, a process essential for handling hydrogen as a clean energy source. Liquefying hydrogen requires temperatures below 20 K, a range where magnetic refrigeration provides temperature control and cyclability. The performance of such systems depends on the use of materials with large magnetocaloric responses near the target temperature.

1.2 Magnetocaloric Effect

The magnetocaloric effect is a thermodynamic process whereby changing an applied magnetic field induces a change in temperature of the material. This relationship arises from coupling between magnetic and thermal degrees of freedom as demonstrated by the change in magnetic entropy.[2-5] On one hand, if done adiabatically, the magnetic moments align with the applied field reducing the disorder of the system which has to be compensated by an increase in lattice entropy and as such in temperature. On the other hand, adiabatically demagnetising the material while the heat is removed via a transfer fluid, results in a decrease in lattice entropy lowering the temperature.

1.2.1 Magnetocaloric cycle

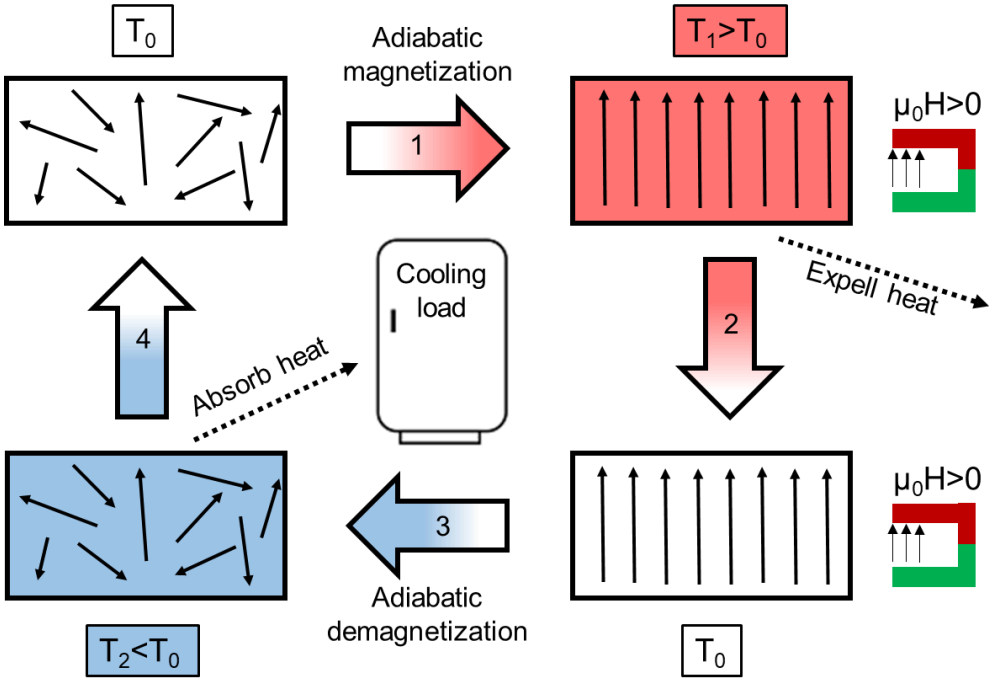

Figure 2: Magnetocaloric cycle[6]

The consequence of this behaviour is the magnetocaloric cycle which enables practical implementation of materials in magnetic refrigeration applications. As illustrated in figure 2, the cycle consists of four steps:

1. **Adiabatic magnetization.** A magnetic field is applied to the material raising its temperature.
2. **Isomagnetic heat transfer.** With the applied field kept constant, the material's excess heat is transferred to a heat reservoir.
3. **Adiabatic demagnetisation.** The field applied to the material is removed, lowering its temperature.
4. **Isomagnetic heat absorption.** The now colder material absorbs the heat from a reservoir completing the cycle.

1.2.2 Hydrogen liquefaction via magnetocaloric refrigeration

In the context of hydrogen liquefaction, where the operating temperatures should be around 20 K, the magnetocaloric effect offers an alternative to conventional systems which are energetically expensive. Magnetocaloric refrigeration at cryogenic temperatures relies on materials exhibiting significant MCE at said temperatures and moderate, not large, magnetic fields.[1,5] The large MCE is evident using two criteria: large adiabatic temperature change and large isothermal entropy change.

Until now the materials with large MCE have mainly been rare-earth-based compounds, which have emerged as leading candidates due to their significant entropy changes and favorable thermal and magnetic properties in the cryogenic regime.

An example would be Holium diboride exhibiting a magnetic entropy change of 40.1 J / kg.K at 5 Tesla with a transition temperature at 15 K.[7,8]

The nature of magnetic ordering dictates the strength and type of magnetocaloric effect at hand. Strong ferromagnetic exchange interactions and narrow hysteresis loops exhibit large isothermal entropy changes near their magnetic transition temperature.

Despite materials like HoB_2 remaining currently exemplary due to their superior magnetic properties, the use of a rare earth metal for magnetic refrigeration presents long term challenges in terms of sustainability and high cost. Alternatively, the desired properties are often exhibited by layered metal hydroxides, which we focus on in this thesis and the general features of which are discussed below.

1.3 Layered Metal Hydroxides

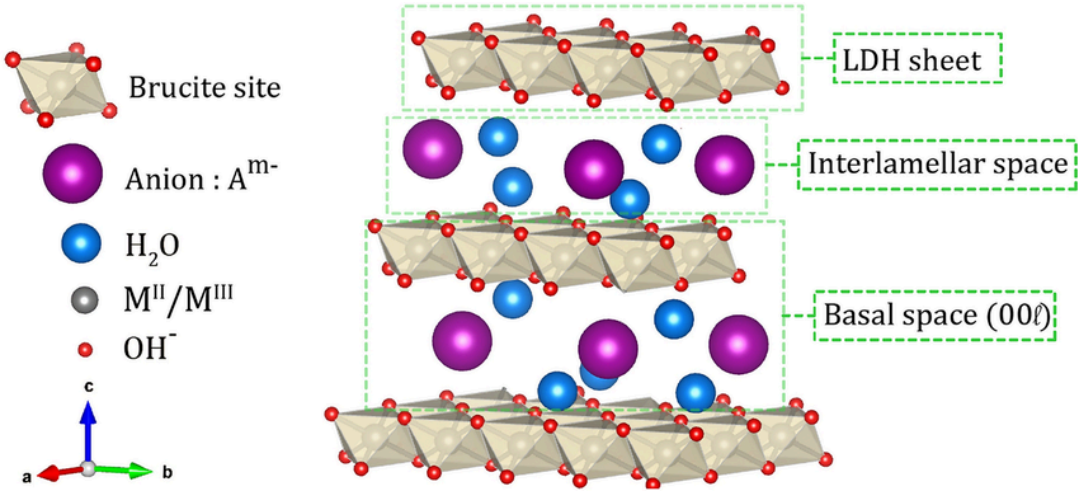

Figure 3: General structure of a layered metal hydroxide[9]

Layered metal hydroxides (LMH) are a diverse class of materials, the structure of which is characterized by edge sharing metal hydroxide octahedra forming two-dimensional brucite-like layers as illustrated in figure 3. The sheets are separated with intercalated ions and water molecules depending on the type of layered metal hydroxide. The layered structure intrinsically comes with pronounced anisotropy making this class of materials highly tunable via intercalation of ions and modification of magnetic behaviour; both of which result in layered metal hydroxide having a broad range of applications.

1.3.1 Layered Simple Hydroxides

Layered simple metal hydroxides (LSH) consist of a monovalent metal coordinated by hydroxide ions in octahedral fashion forming mostly neutral layers. Their structure is often described as being brucite-like, in particular similar to $Mg(OH)_2$, where metal hydroxide octahedra arrange into two dimensional planes separated by an interlayer space with ions and water molecules. Despite structural stability, this subtype of

layered metal hydroxides lacks the flexibility and versatility that are beneficial for tuning magnetic properties limiting their applications.

1.3.2 Layered Double Hydroxides

In contrast, another subtype are layered double hydroxides (LDH), which incorporate two types of metal cations, a divalent cation and a trivalent cation where a portion of the divalent cations is replaced by trivalent cations resulting in positively charged brucite-like layers. In order for the overall structure to remain neutral the charge of the layers needs to be counterbalanced by intercalated anions such CO_3^{2-}, NO_3^-, or Cl^-. The general formula for LDHs is $[M^{2+}_{1-x}M^{3+}_x(OH)_2]^{x+}(A^{n-})_x/\square \cdot yH_2O$, where A^{n-} denotes the interlayer anions and their charge. Having a mixed valent compound broadens the range of tunability when it comes to morphology. As a result, the diverse roster of LDHs demonstrates a wide range of magnetic properties.

1.3.3 Magnetic interactions in layered metal hydroxides

For the materials in question, the modularity of their structure allows incorporations of magnetically favourable cations such as Mn^{2+}, Fe^{3+} Co^{2+} etc. to promote a variety of magnetic interactions such as the superexchange, double exchange, and RKKY interactions.

The specific arrangement of metal cations within two-dimensional brucite-like layers and intercalated ions govern the overall magnetic properties exhibited by layered metal hydroxides. Some of the most notable consequences of said arrangement are superexchange and double exchange mechanisms and Ruderman-Kittel-Kasuya-Yosida (RKKY) coupling whereby affecting the compound's morphology via cationic composition and ion intercalation dictates the ground state of the layered system at hand.

1.3.3.1 Superexchange

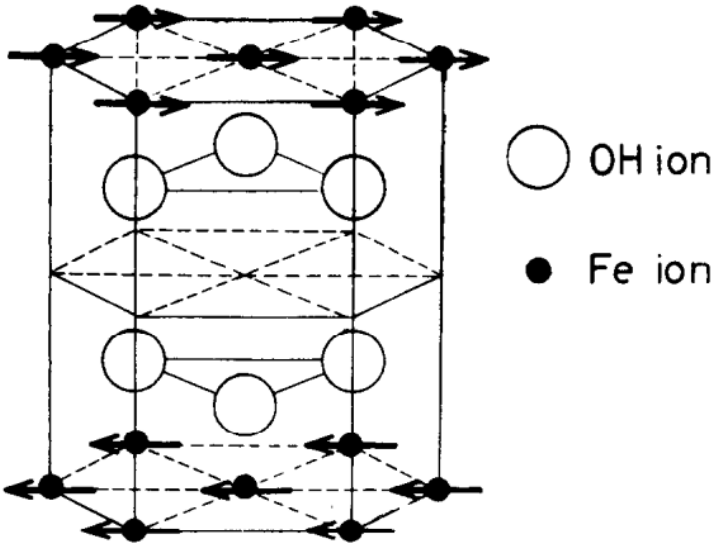

Figure 4: Structure of $Fe(OH)_2$[10]

In LMHs, the metal cations are octahedrally coordinated by hydroxide anions and the resultant octahedra are arranged in a brucite-like fashion sharing edges with each other. In the absence of direct overlap between the d-orbitals of metal cations, the spins of individual metal centers can communicate via hydroxide bridges via the superexchange mechanism. This interaction is affected by the angle created by two metal centers and a hydroxide bridging the two, orbital symmetry and the electronic configuration of the metal cations involved. For instance, in the case of $Fe(OH)_2$ Fe^{2+} cation favour ferromagnetic superexchange via bridging hydroxide ions which results in ferromagnetic coupling within a layer with the material being antiferromagnetic overall as a result of dipole-dipole interactions between the layers.[10] Because LMHs are layered systems, the superexchange is anisotropic and for an antiferromagnetic system this comes with a degree of magnetic frustration.

1.3.3.2 Double exchange

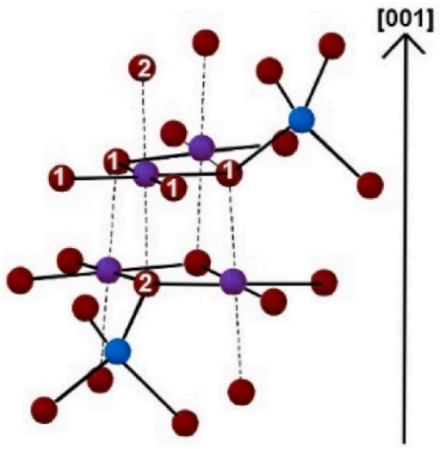

Figure 5: Structure of octahedral and tetrahedral sites in hausmannite[11]

Whenever layered metal hydroxides possess metal cations of mixed valence such Fe^{3+}/Fe^{2+}, electrons can partially delocalize between cations of differing valency through bridging ligands allowing for electron hopping. The mechanism by which the delocalization occurs is known as the double exchange mechanism which is energetically favourable when the magnetic moments are parallel, thus resulting in ferromagnetic interactions within metal hydroxide layers. This concept is exemplified with manganese-based mixed oxide, Mn_3O_4, known as hausmannnite where the tetrahedral sites are occupied by Mn^{2+} and the octahedral sites are occupied by Mn^{3+} and partially Mn^{4+} cations. The double exchange occurs between octahedral sites such that electrons hop between Mn^{3+} and Mn^{4+} cations via oxygens.[11] In LDHs, the mixed valency of metal cations can be controlled via redox environments, interlayer ions and pH allowing to alter the magnetic transition temperatures to suit the application.

1.3.3.3 Ruderman-Kittel-Kasuya-Yosida (RKKY) coupling

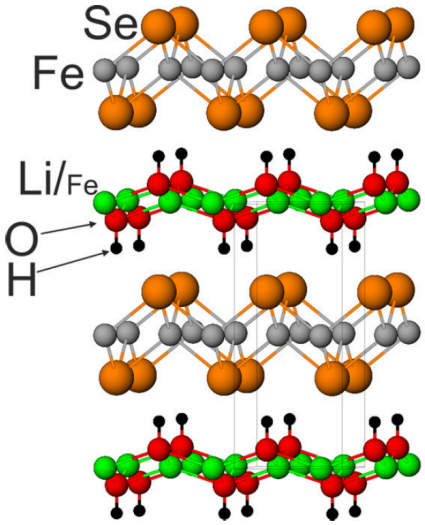

Figure 6: Layer structure of $Li_{1-x}Fe_x(OH)Fe_{1-y}Se$. The unit cell is also highlighted.[12]

While less common, the RKKY interaction becomes relevant in hybrid systems which include itinerant carriers intercalated in the structure. Incorporating a conductive interlayer species, such as organic π systems and redox active anions, may allow localized magnetic moments to couple indirectly via conduction electrons. In particular systems like $Li_{1-x}Fe_x(OH)Fe_{1-y}Se$, illustrated in figure 6, a postsynthetic lithiation introduces further Li into the system to displace iron cations from the hydroxide layer which fills iron vacancies in the FeSe layer which promotes the superconductivity.[12] Furthermore, the iron in the hydroxide layers enhances the transition temperature by increasing charge transfer of electrons into the FeSe layers supplying a level of doping comparable to that in metal/ammonia intercalates. Overall hybrid or doped systems benefit from this mechanism broadening the overall tunability of their properties whereby picking the right metal cations and interlayer ions the RKKY interaction can be exploited to further enhance the long range magnetic order present.

1.3.3.4 Interplay between the mechanisms

The balance among these interactions strongly influences the magnetic ordering observed in LMHs. Superexchange stabilizes antiferromagnetic or weakly ferromagnetic states at low temperatures, while double exchange can induce ferromagnetism in mixed-valent layered systems. The inherently low dimensionality hinders long-range magnetic order, reducing the transition temperature which is advantageous for hydrogen liquefaction due to the cryogenic temperatures being needed for operation. Whereas RKKY interaction facilitates electron delocalization via interlayer species which favours AFM or FM ordering depending on the interlayer distance.

The combination of double exchange, superexchange and RKKY interactions directly affects the magnetocaloric properties of layered metal hydroxides. In particular a large magnetocaloric effect is characterized by a large magnetic entropy change near a magnetic phase transition which occurs whenever the spins align cooperatively which can be induced via double exchange, generally favouring

ferromagnetic arrangement within the brucite-like layers. Antiferromagnetic layered metal hydroxides, however, are governed by the superexchange mechanism with MCE of smaller magnitudes as AFM ordering cannot in general be induced by an applied magnetic field.

1.3.4 Advantages of using LMHs for MCE

The principal advantage of using ferromagnetic layered metal hydroxides in magnetocaloric applications is the narrow hysteresis. Furthermore, their modularity via tuning of the cationic ratio, layer stacking, and interlayer chemistry offers pathways to optimize the balance between magnetic interactions, thermal and air stability along with the overall magnetocaloric behaviour.[13-16] Since the interlayer space can accommodate various ions which influence the magnetic coupling between layers but also serve as means of adjusting interlayer spacing tied to the type of ordering. Additionally, the capacity for ion exchange or exfoliation creates opportunities for creating composite materials with enhanced thermal, catalytic and magnetic responses.

1.3.5 Disadvantages of using LMHs for MCE

However, a set of challenges limit the potential of this family of materials in magnetic refrigeration. Compared to conventionally used materials for magnetocaloric applications such as hydrogenated gadolinium, LDHs and LSHs possess a lower density of magnetic ions per unit cell resulting in lower efficiency. Another challenge associated with these materials is their sensitivity to air and moisture inducing decomposition of layered metal hydroxides into related hydroxide salts and minerals.

1.3.6 Research motivation

In spite of said challenges, layered metal hydroxides generally exhibit narrow hysteresis loops allowing for faster cycling between states when implemented within a refrigeration device. Additionally, these layered systems have low transition temperatures which are favourable for operation applied to hydrogen liquefaction. The structures can be modulated via tactical use of spacer ions to control inter-plane interactions, whereby increasing the layer spacing tends to support ferromagnetic ordering. Furthermore, introducing magnetically favourable cations to control interactions within the layers increases the overall effective magnetic moment per metal cation, and improves the magnetic entropy change, crucial to efficient magnetic refrigeration. Layered metal hydroxides are promising candidates which serves as a motivation for investigating a series of monometallic mono and multivalent systems. The systems researched incorporate a variety of manganese, iron or cobalt cations with the aim of promoting double exchange within the layers while taking advantage of tunable layer spacings via intercalated anions in order to favour ferromagnetic inter-layer interactions. The synthetic products are characterised by powder and single crystal X-Ray diffraction techniques while magnetometry is conducted to test the viability of the materials of interest in magnetocaloric applications without involving the use of rare earth metals.

2. Methods

2.1 Synthesis of Manganese based layered double hydroxides

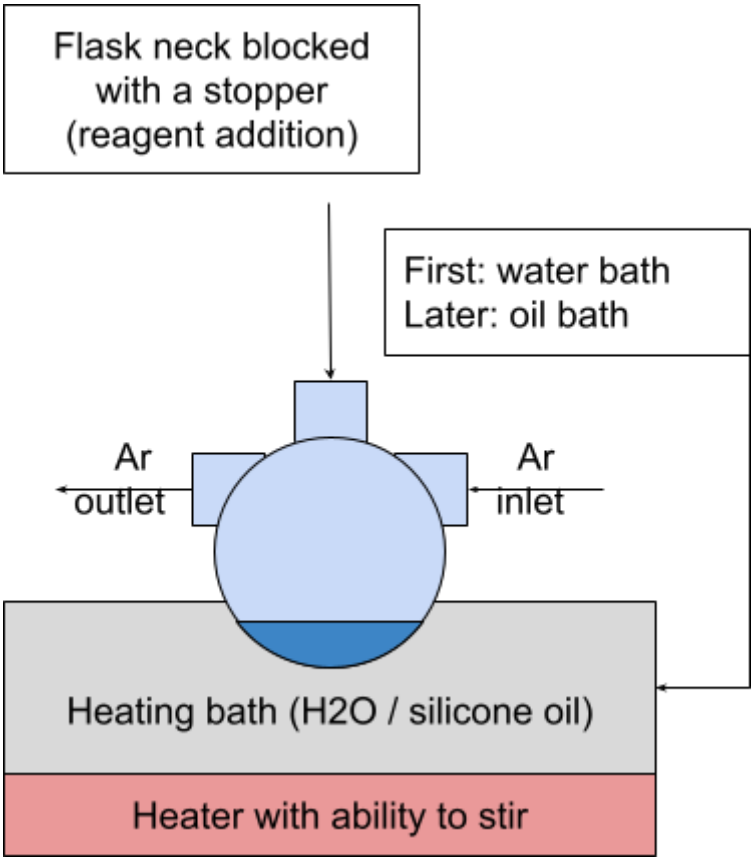

Figure 7: Product and setup photos

$$MnSO_4 \bullet H_2O + NaOH \rightarrow Mn - LDH + Mn_3O_4 + Na_2SO_4$$

Manganese-based layered double hydroxide (Mn-LDH) was prepared via solvent evaporation varying aspects of the system such as temperature, time, reagents and means of purification. First, the setup, depicted in figure 7, was purged with argon (later with nitrogen) and subsequently NaOH (1.77 g, 44 mmol) was added to 10 ml of deionized water. Following that $MnSO_4.H_2O$ (5.0 g, 30 mmol) was added to the flask and the mixture was left stirring for 90 minutes. Known as the R value, the ratio of [-OH] / [Mn^{2+}] was kept at ~1.5 to favour the formation of layered double hydroxides instead of manganese hydroxide and Mn_3O_4 (hausmannite) which would form when deviating from said ratio.[17,18] Once reacted, the reaction mixture was heated to 80 °C and left under argon overnight to evaporate the water or placed inside a vacuum oven at the same temperature. In later attempts, a purification step was introduced whereby washing the product with 1% sulfuric acid using a funnel allowed various non-magnetic impurities such as sodium sulfate to be washed away.[19-21] Lastly, a recrystallization step was added during later experiments in an attempt to crystallize the product, which was done by dissolving the polycrystalline product in 20 ml of 1% sulfuric acid and leaving the mixture at 80 °C under argon until the liquid had evaporated.

Table 1: Conditions used for synthesis of Mn-LDH

Batch	T_{evap} (℃)	Washing	Recrystallization	$T_{recryst}$ (℃)	Main Product
1	**100**	✗	✗	**N / A**	Mn-LDH-1 Mn-LDH-2 Na_2SO_4
2	**80**	✗	✗	**N / A**	Mn-LDH-1 Mn-LDH-2 Na_2SO_4
3.1	**100**	✗	✗	**N / A**	Mn-LDH-1 Mn-LDH-2 Na_2SO_4
3.2	**100**	✓	✗	**N / A**	Mn-LDH-2 Na_2SO_4
4	**100**	✓	✓	**150 (Argon)** **100 (Air)**	$Na_2MnSO_4 \cdot 2\ H_2O$ Na_2SO_4
5	**100**	✓	✓	**115 (Argon)**	N / A (corrosive; unstable)
6	**100**	✓	✓	**115(Argon)**	N / A (corrosive; unstable)
7	**100**	✗	✓	**115(Argon)**	Mn-LDH-1

2.2 Synthesis of Green Rust, $[Fe^{II}_{0.33}Fe^{III}_{5.67}(OH)_{12}] \cdot 3[C_3H_5O_3] \cdot 1.33[CO_3]$

$$FeCl_3 \cdot 6\,H_2O + Na^{+}\,^{-}OCCH_3 \rightarrow Green\ Rust + Fe_3O_4 + Fe(O)OH + NM\ side\ products$$

$$C_3H_5(OH)_3 \rightarrow C_3H_4(OH)_2O \rightarrow C_3HCOCHO \rightarrow CH_3CHOHCOO^{-}\ (\ lactate\ anion\ )$$

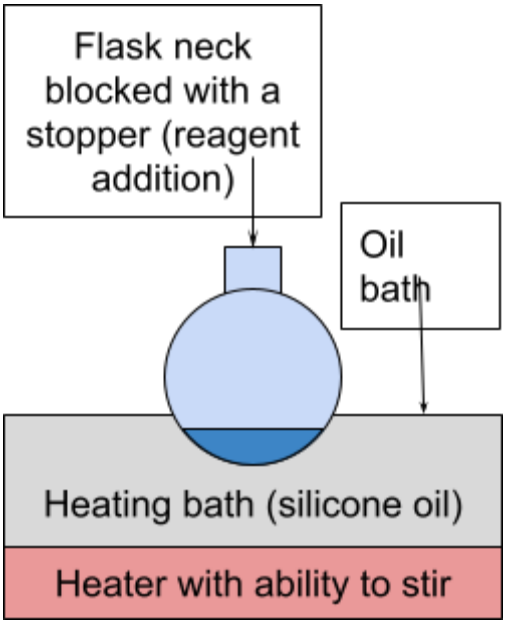

Figure 8: Product and setup photos

Green Rust, an iron based layered double hydroxide, was synthesised by first adding 100 ml of glycerol to a round bottom flask equipped with a magnetic stirrer.[22-26] Subsequently, sodium acetate NaO_2CCH_3 (7.2 g, 8 mmol) was added to the flask and stirred until homogeneity. Following that $FeCl_3 \bullet 6H_2O$ (4.5 g, 2 mmol) was added and the mixture was set to stir at 80 °C for 90 minutes. Once complete, the reaction mixture was transferred to a Teflon-lined insert which was then placed in an autoclave for solvothermal treatment, whereby via the decomposition of glycerol the resultant product would be air stable. The autoclave was transferred to a Pol-Eko low temperature oven for varying lengths of time with 5 hours ramp-up and 5 hours ramp-down. Once cooled to room temperature, the sample was collected and washed four times: once with pure ethanol, twice with a 1:1 ethanol: DI water mixture, and once more with pure ethanol. Having been washed, the sample was left to dry on a heating plate at 100 °C for 4 days or inside a vacuum oven at 90 °C for 2 days.

Table 2: Conditions used for synthesis of Green Rust

Batch	Synthesis	$T_{synthesis}$ (℃)	Time	Drying	T_{dry} (℃)	Time	Washing
1	Solvothermal	200	24 h	Heating plate Vacuum oven	100	1 week + 1 week	None
1	Solvothermal	200	24 h	Heating plate Vacuum oven	100	1 week + 3 days	PropOH
2	Solvothermal	200	48 h	Vacuum oven	100	0 days + 2 days	EtOH:H2O
3	Solvent evaporation	170	72 h	Heating plate	100	0 days + 2 days	EtOH:H2O

2.3 Synthesis of layered simple hydroxide, $[Fe(OH)_2CH_3CHOHCOO^-] \bullet H_2O$

$$FeSO_4 \cdot 7\,H_2O + NaOH \rightarrow Fe - LSH + Fe_3O_4 + Na_2SO_4$$

$$C_3H_5(OH)_3 \rightarrow C_3H_4(OH)_2O \rightarrow C_3HCOCHO \rightarrow CH_3CHOHCOO^- \ (\,lactate\ anion\,)$$

To test the viability of utilising glycerol decomposition to stabilise air sensitive layered systems, an iron based layered simple hydroxide containing only Fe(II) cations was prepared (referred to as Fe-LSH).[22] First, NaOH (2.5 g, 60 mmol) was added to a round bottom flask containing 100 ml of glycerol at 80 °C which was left stirring until homogeneity was achieved. Subsequently, $FeSO_4 \bullet 7H_2O$ (13.9 g, 50 mmol) was transferred to the round bottom flask and the reaction was left at 80 °C for 90 minutes. Upon completion, the reaction mixture was transferred to a Teflon-lined insert which was placed inside an autoclave for solvothermal treatment. After solvothermal treatment for 4 days at 150 °C, the product was poured into a funnel where it was washed once with pure ethanol, twice with a 1:1 mixture of ethanol and deionized water, and lastly once with pure ethanol such that each wash required 100 ml of solvent. Once washed, the sample was dried in a vacuum oven at 80 °C for 3 days. Taking into account the results of magnetic measurements on this compound (see below), an attempt was made to treat the synthesized product with a mixture of 5% hydrogen and 95% argon to induce reduction. The product was crushed and transferred to a small crucible which was placed in a tube furnace for 24 hours at 100 °C under the flowing gas mixture.

2.4 Synthesis of cobalt-based Layered Double Hydroxide, $Co_5(OH)_6(SeO_4)_2 \bullet 4H_2O$

To synthesise $Co_5(OH)_6(SeO_4)_2 \bullet 4H_2O$, the procedure was optimised to limit the amount of time the intermediate and final products were exposed to air so as to avoid oxidation of Co^{2+}.[27] The setup consisted of a heating plate with an oil bath in which a three-necked flask was submerged for uniform temperature control. Initially, while the setup was being purged with nitrogen for 30 minutes, 40 wt% solution of selenic acid (3 ml, 8 mmol) and cobalt carbonate (1 g, 8 mmol) were weighed out. Once the solution was purged, the reagents were transferred to the flask along with 10 ml of deionized water and then the reaction was left stirring under nitrogen at 30 °C for 1 hour. Following that, the stirring was turned off and the temperature was increased to 100 °C for several days to evaporate the water. The resulting dried pink crystals of cobalt selenate pentahydrate were collected and 1.2 g were weighed out, crushed and transferred to a flask containing 15 ml of deoxygenated deionized water. Separately, NaOH (0.1 g, 2.5 mmol) was weighed out and dissolved in 15 ml of deionized water. The two solutions were mixed under nitrogen and the resultant blue suspension was transferred to a Teflon-lined insert which was placed in an autoclave. Subsequently, hydrothermal treatment of the reaction mixture was performed at 150 °C for 48 hours with a 12 hour ramp-up and 3 hour ramp-down. The top layer of water was then decanted and the rest was transferred to a funnel and washed with ethanol, acetone and deionized water. After washing, the product was dried at 40 °C for 1 hour yielding a uniform pink powder.

2.6 X-Ray Diffraction

The samples obtained throughout the project were analysed via powder XRD to identify the products formed and via single crystal XRD to characterize previously unknown products.

In particular, powder XRD measurements were performed on a Bruker D8 Endeavour diffractometer from 5 to 55 degrees 2Θ with a step size of 0.02 degrees, which captures the low angle peaks characteristic of layered systems, while the high angle peaks are integral to identifying unused reagents, side products and undesired minerals. The samples were prepared by crushing the product in a mortar until a fine powder was obtained which was transferred to a PMMA sample holder ensuring an even spread of material.

The obtained diffraction patterns were analysed using two programs: Profex5 and EXPO2.[28-29] Profex5 is a program that performs a variety of refinement protocols to identify the compounds present in the product along with their relative proportions with respect to each other. Should Profex5 not be able to identify all the peaks present, EXPO2 can be used to determine the unit cell if peaks belonging to any impurity phases identified by Profex5 could be excluded.

2.7 Magnetometry

In order to assess the potential of layered metal hydroxides in magnetocaloric applications, magnetic measurements were performed using a SQUID magnetometer (Magnetic Properties Measurement System (MPMS)). The samples were prepared by placing around 8 mg of product in a transparent gelatin capsule filled with cotton. The capsule was placed inside a plastic straw which was subsequently attached to the sample holder rod that is placed inside the machine.

2.7.1 Protocols used

A variety of protocols were used to assess how the magnetisation of the product changes with temperature and applied field (referred to as M-T and M-H measurements). The M-T measurements followed the Zero Field Cooled / Field Cooled procedure, where the sample was first cooled from 300 K down to 5 K without a field applied. Subsequently, a field of 0.1 T was applied and the sample was heated from 5 K to 300 K, known as the ZFC protocol. Without turning off the field, the sample was cooled back down to 5 K and then heated to 300 K while measuring, known as the FC protocol. The data collection is done by measuring the DC current generated. The M-H measurements were performed to assess the coercivity, remanent and saturation magnetizations, which give an insight into the cyclability, magnetic entropy change and relative cooling power. Using the same sample preparation as for the M-T measurements, the M-H scans were performed at fixed temperature by sweeping the field applied to the material from - 5 T to +5 T with a step size of 0.01 T between -1 T and + 1 T, and a step size of 0.1 T for the ranges - 5 T to -1 T and 1 T to 5 T. To calculate the magnetic entropy change, M-H scans should be performed over a range of temperatures below and above the transition temperature with a step of 1 K.

2.7.2 Data analysis

The magnetometry data obtained in units of emu were adjusted to account for the diamagnetic contribution which is always present and is dependent on all the ions in the product. Once adjusted, the M-T curves were inspected to identify the point of largest change in slope, which often corresponds to the onset of long-range magnetic ordering: the Néel temperature for antiferromagnetic materials or the Curie temperature for ferromagnetic materials.

The magnetic susceptibility was calculated by dividing the magnetisation (emu per mole) by the measuring field (Oersted, see equation 1).

$$\chi = \frac{M}{H} \tag{1}$$

Subsequently, plotting the inverse of the susceptibility against temperature yields a graph that is linear in the paramagnetic temperature region. Fitting this region with a straight line (Equation 2) and extrapolating gives a gradient of $1/C$ and an intercept with the x-axis of θ_W, where C is the Curie constant and θ_W is the Weiss temperature which can be interpreted as follows:

- If $\theta_W > 0$, the material has ferromagnetic interactions.
- If $\theta_W < 0$, the material has antiferromagnetic interactions.
- If $\theta_W = 0$, there are no magnetic interactions.

The Curie constant can be used to estimate the effective magnetic moment (μ_{eff}) per magnetic atom in accordance with equations (3) and (4) (for the example of a compound containing n Co^{2+} and m Co^{3+} ions per formula unit).

$$\frac{1}{\chi} = \frac{T}{C} + \frac{\theta_w}{C} \tag{2}$$

$$\mu_{eff} \approx \sqrt{8 \cdot C} \tag{3}$$

$$\mu_{eff} = \sqrt{\left(n\mu^2_{Co^{2+}} + m\mu^2_{Co^{3+}}\right)} \tag{4}$$

Comparing these experimental values with the theoretical spin-only effective moment (Equation 5) allows the valency of the metal cations involved to be determined, providing insight into which magnetic interactions dominate in the material. Furthermore, equation 6 can be used to estimate the ratio of oxidation states of the metal responsible for the magnetic response, where n is the fraction of a given oxidation state, and $\mu(M^{2+/3+})$ is the spin-only magnetic moment for a given oxidation state calculated from the number of unpaired electrons, N.

$$\mu_{eff} = \sqrt{N \cdot (N + 2)} \tag{5}$$

$$n_{2+} = \frac{\mu_{eff} - \mu_{y+}}{\mu_{x+} - \mu_{y+}} \tag{6}$$

$$\Delta S_M = \sum_j \frac{M(T_{i+1}, H_j) - M(T_i, H_j)}{T_{i+1} - T_i} \cdot \Delta H_j \tag{7}$$

In order to assess the viability of a given material in a cooling device for hydrogen liquefaction, the magnetic entropy change ΔS_M serves as an indirect way to describe the magnitude of the magnetocaloric effect. The magnetic entropy change can be calculated by obtaining M-H data at a range of different temperatures close to the magnetic ordering transition, and applying Equation 7.

3. Results and Discussion

3.1 Manganese layered double hydroxide

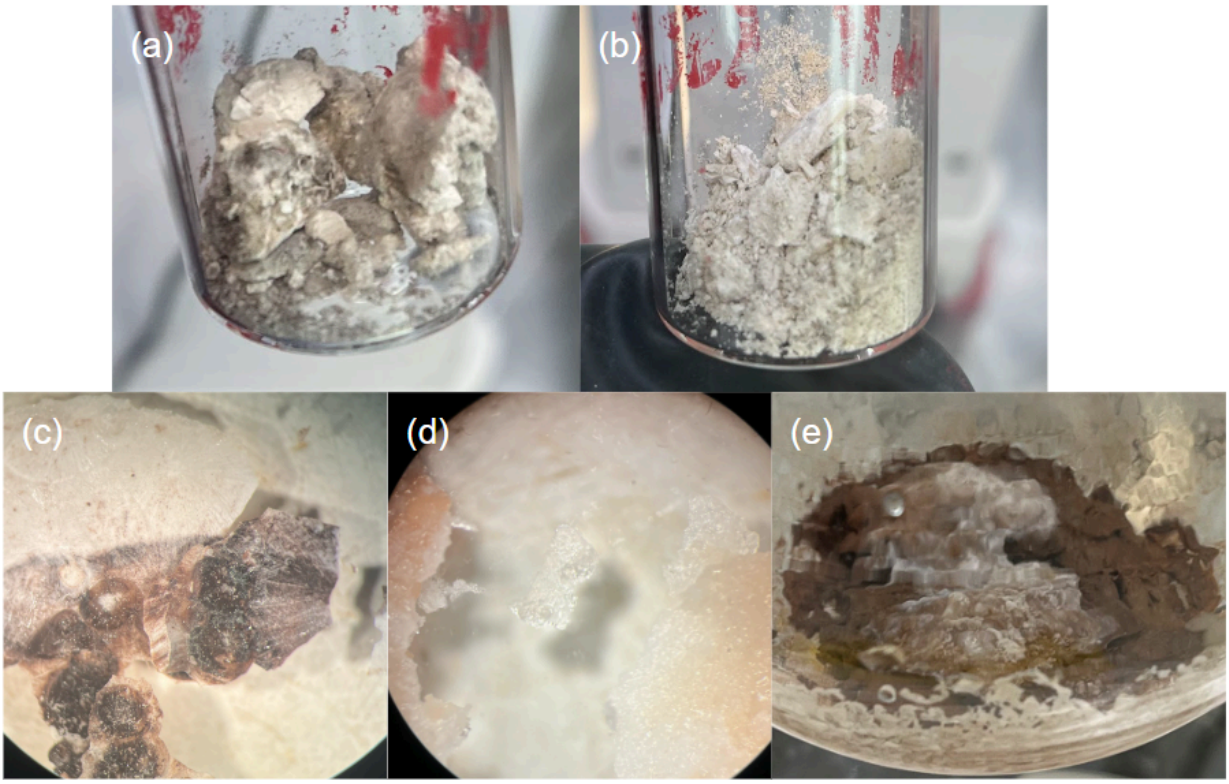

Figure: 9 Product photos of (a) Batch 3.1, (b) Batch 3.2, (c) Batch 4, (d) Batch 5, (e) Batch 7

The first compound was previously synthesized in the group from manganese sulfate monohydrate and sodium hydroxide. The reagents were transferred to a flask with sodium sulfite, added for chemical dehydration of the sample, to yield a ferromagnetic layered double hydroxide system after evaporating at 60 ℃ overnight.

Synthesis. Initially a batch prepared via solvent evaporation under argon was collected as a wet white precipitate with regions of brown indicative of hausmannite being formed as a side product, whose presence will affect magnetic measurements given its AFM behaviour(batch 1 and 2). While an excess of sodium hydroxide is necessary for the formation of the desired LDH phase, it is also vital to work under an inert atmosphere as when given exposure to air, manganite becomes the majority product as Mn-LDH decomposes. Given the outcome, the procedure was adapted to improve the purity of the product by washing the sample after the solvent had been evaporated(batch 3.1 and 3.2). To avoid introducing new

ions into the solution, the product was washed with ~1% sulfuric acid resulting in a brownish powder, the color of which is attributed to formation of manganite driven by decomposition of LDH via oxidation of manganese cations in air.

Given the potential applications, synthesising single crystals of Mn-LDH would be beneficial for magnetocaloric applications since presence of nonmagnetic impurities affects the rigidity of the structure while magnetic impurities affect the magnetic properties. Thus the procedure was adapted to attempt the recrystallization of Mn-LDH after washing. The product collected after washing was dissolved in 20 ml of ~1% sulfuric acid with 2 ml of 10% sulfuric acid added for improved solvation. During the first attempt of this procedure, the argon gas ran out and the gas outlet was too narrow hindering the recrystallization efforts(batch 4). To speed up the process, excess acid was decanted and the solution was exposed to air to improve evaporation. After 3 days two distinct phases were collected: black crystals and white powder. The repeat attempts did not yield the black crystals and instead yielded a mixture of manganite and corrosive white material implying that it was a hard-to-reproduce assortment of factors that resulted in black crystals in the first attempt(batch 5 and 6). Since exposure to air is undesirable for the synthesis and purification of Mn-LDH, a procedure without washing was implemented which yielded a brown and white mixed phase product and failed to generate single crystals (batch 7).

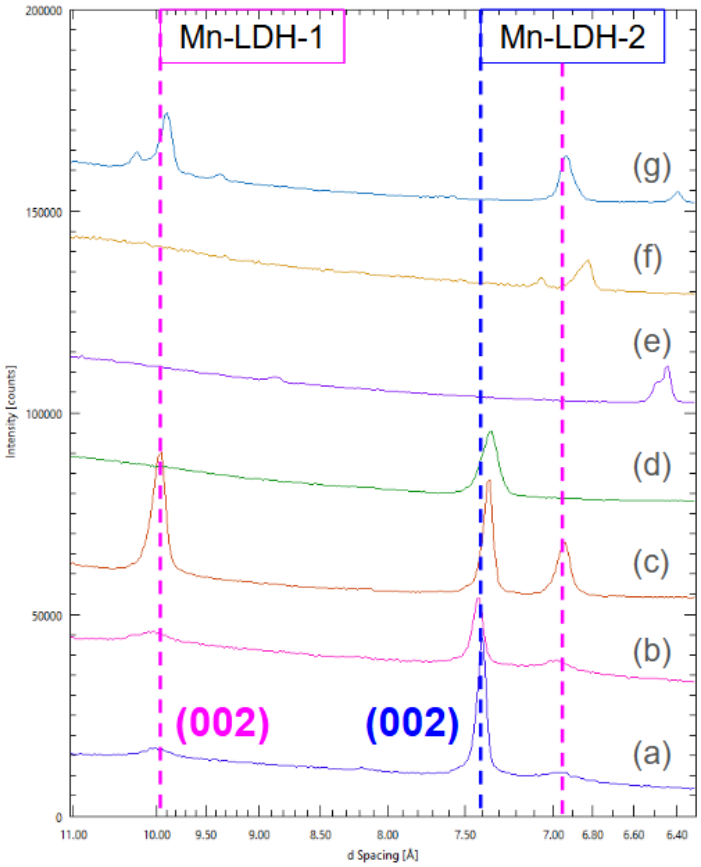

Figure 10: Powder XRD patterns of characteristic peaks for (a) Batch 1, kept in air; (b) Batch 2, glovebox; (c) Batch 3.1, prior to wash; (d) Batch 3.2 washed with H_2SO_4; (e) Batch 4, black crystals; (f) Batch 5, recrystallization; (g) Batch 7, recrystallization, no wash. The peaks used to identify Mn-LDH-1 and Mn-LDH-2 are labeled with pink and blue dashed lines respectively.

3.1.1 Structural investigations. X-Ray Diffraction:

All of the powder XRD measurements were performed from 5 to 55 degrees 2Θ using a step size of 0.02 degrees 2Θ, taking 1.5 hours for each measurement. The initial batch of the product was split in two, keeping one half in a nitrogen-filled glovebox (batch 1b) and the other half in air (batch 1a). Both patterns show the presence of the crystalline compound as demonstrated by a peak at 12 2Θ as the lowest angle peak is caused by 001 or 002 peaks for layered systems.[27,30] Using Profex5 the main impurity phases were identified as sodium sulfate, hausmannite.

The next attempt utilising the same synthesis procedure yielded pattern (b), similar to pattern (a) indicating general reproducibility of the product. Worth noting is the variance in ratios between the three lowest angle peaks, suggesting the presence of multiple phases in the product. To get a better understanding of the products formed, EXPO2 was used to approximate the unit cell parameters of the suspected LDH phases.

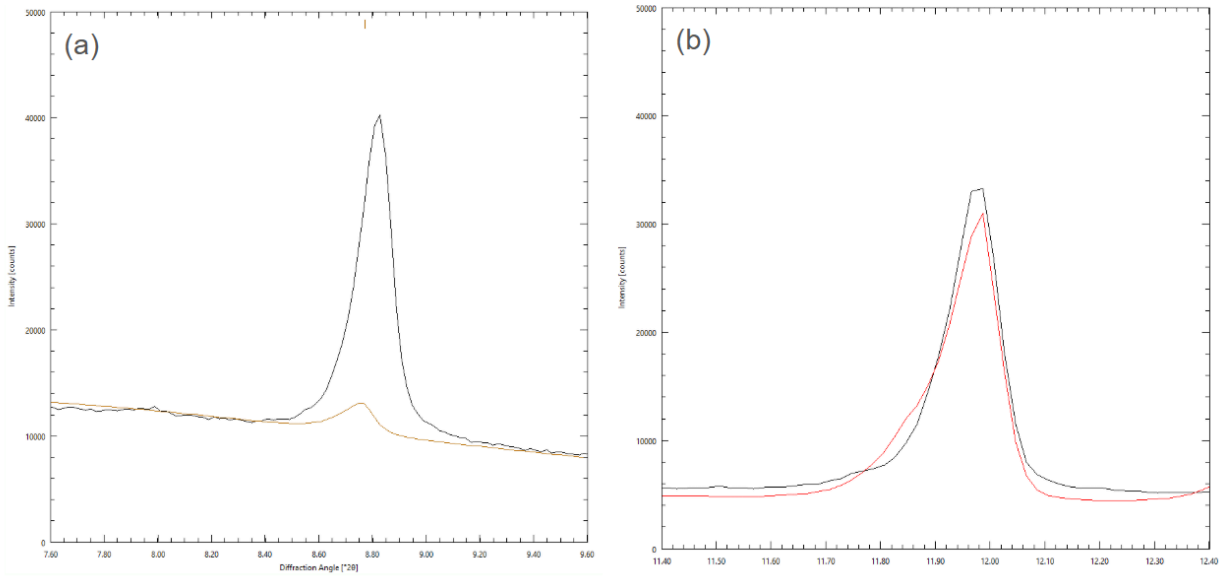

Figure 11: Fitting of adapted unit cells for (a) Mn-LDH-1 and (b) Mn-LDH-2.

Given the lattice parameters calculated, two existing structures in the literature, $Fe_2(H_2O)_4[(SO_4)_2O]$ 4 H_2O and $Fe(OH)_3(SO_4)$, were modified in an attempt to analyse the intensities of the peaks (see Table 3). The first structure, labeled Mn-LDH-1, is likely to be a triclinic P-1 layered hydroxide compound; this phase accounts for the peaks at 8.8° 2Θ and 12.7° 2Θ observed in several of the XRD patterns; the high intensity of the 00l peak is due to the preferred orientation commonly found for polycrystalline samples of layered systems. The peak at 11.9° 2Θ can be accounted for by a second phase, labeled as Mn-LDH-2.

Table 3: Modified parameters of $Fe_2(H_2O)_4[(SO_4)_2O]$ $4H_2O$ and $Fe(OH)_3(SO_4)$ for Mn-LDH-1 Mn-LDH-2

Material that was modified	Lattice parameters			Lattice angles		
	a (Å)	b (Å)	c (Å)	α	□	γ
$Fe_2(H_2O)_4[(SO_4)_2O]$ $4H_2O$	8.70	10.29	7.50	94.688°	96.517°	97.240°
$Fe(OH)_3(SO_4)$	6.50	7.37	5.84	90°	108.38°	90°

During later trials, the XRD patterns of the products were taken before and after washing with ~1% sulfuric acid. Approximating the composition of the product using Profex5 indicates that prior to acid treatment the combination of Mn-LDH-1 and Mn-LDH-2 accounted for 20% (molar) of the sample. Comparing XRD patterns, it is apparent that there are two layered compounds forming as the relative intensity of peak at 12 degrees 2Θ has not changed with respect to the Mn_3O_4 (hausmannite) peak at 36 degrees 2Θ. In contrast, the first and third lowest angle peaks disappeared after washing implying that LDH-1 is more soluble in sulfuric acid than LDH-2.

3.1.2 Recrystallization attempts

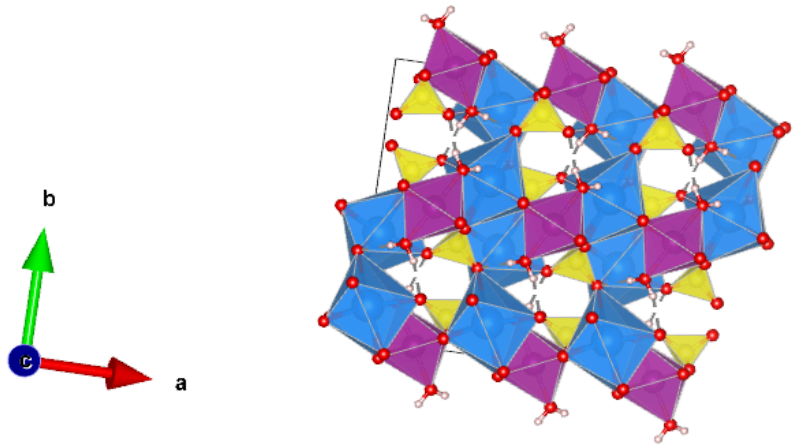

Figure 12: Crystal structure of $Na_2Mn(SO_4)_2{\cdot}2H_2O$ solved using SC XRD

Given the lack of success with obtaining single crystals of the material large enough for measurement by SCXRD, an attempt was made to dissolve and recrystallize the product in ~1% sulfuric acid. As mentioned in the synthesis section, a variety of factors went wrong requiring that the flask be exposed to air and excess acid be decanted. In spite of these issues, the procedure yielded donut-shaped black crystals which were analysed via SC XRD to identify the compound as $Na_2Mn(SO_4)_2{\cdot}2H_2O$, the structure of which is shown in figure 12, which has been reported in the literature with the same space group as obtained via SC XRD, P 1 21/c 1, with the lattice parameters given in Table 4.[32] Given the fact that this product is not a layered system, the discussion of the black crystals' magnetic properties comes at a later point.

Table 4: Refined lattice parameters for $Na_2Mn(SO_4)_2 \cdot 2H_2O$ solved using SC XRD

a (Å)	b (Å)	c (Å)	α	□	ɣ
5.78370	12.95120	5.48540	90.0000°	106.2090°	90.0000°

Since a variety of factors deviated from the planned procedure in the initial crystallisation attempt, the procedure was performed twice as intended to probe the reproducibility of the results. The powder XRD patterns for these subsequent attempts indicate that the reagents, the two Mn-LDH phases and the previously observed Mn-based oxide impurities do not account for the majority of the peaks. The repeat attempts yielded another unidentified product (pattern (f)), different to $Na_2Mn(SO_4)_2 \cdot 2H_2O$ implying that the factors that went wrong during synthesis were integral to formation of these crystals. Given the results thus far, washing was an effective method to remove one of the main product phases and to reduce the amount of side products relative to the main product. Nonetheless exposure to air during washing could induce oxidation or decomposition; thus as a final adjustment to the procedure, the washing step was removed in order to reduce the exposure to air to avoid oxidation of Mn^{2+} cations. Based on the powder XRD pattern obtained, the sample obtained via recrystallization without washing is a mixture of previously synthesised Mn-LDH-1, sodium sulfate, hausmannite and two other phases as evidenced by the peaks at 8.57° 2Θ and 9.37° 2Θ.

Given the variety of conditions changed throughout, the reactivity of manganese cations is affected by the reagents used, temperature, concentrations of sulfate and hydroxide anions, and redox processes making it difficult to control the nature of the final product and to limit the formation of side products.[31] The sulfate to hydroxide ratio can change in solution, affecting the manganese oxidation state, while the affinity of sodium cations for sulfate yields large quantities of sodium sulfate as a side-product.

3.1.3 Magnetometry

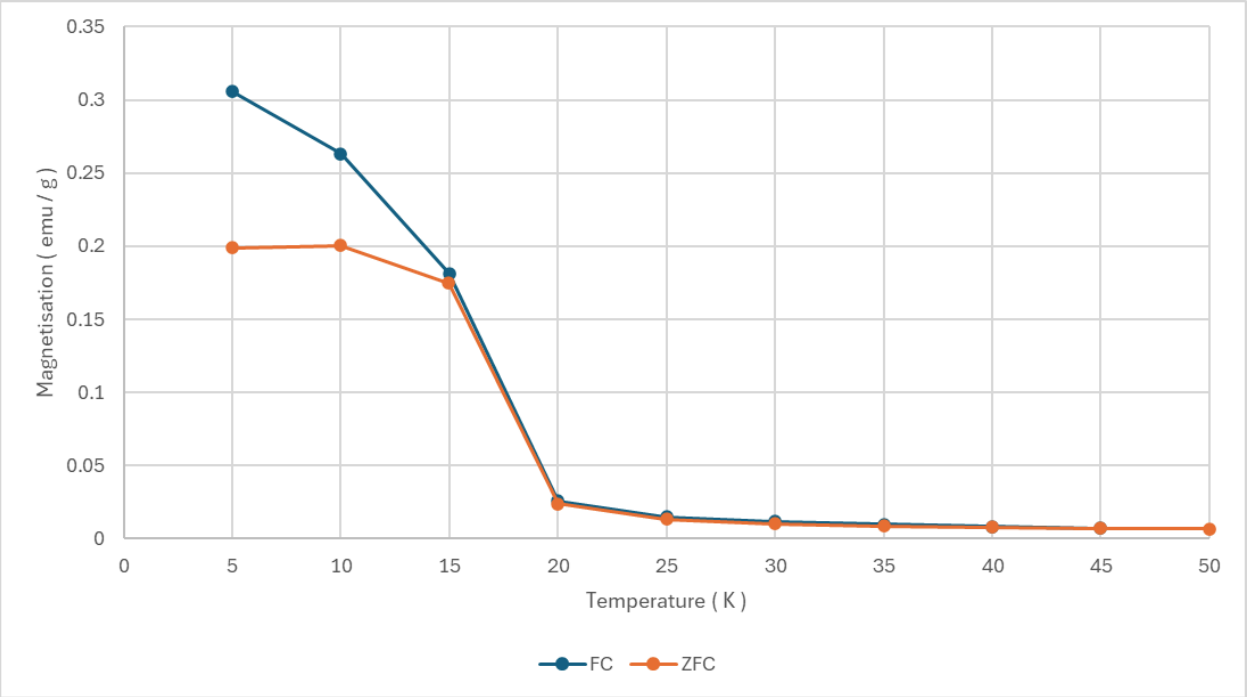

Figure 13: M-T ZFC/FC data for Batch 3Mn-LDH prior to introduction of the washing step

Magnetisation versus temperature (M-T) scans were performed on warming from 5 K to 300 K with an applied field of 0.01 T. These measurements were performed on the sample from Batch 3 with Mn-LDH-1 and Mn-LDH-2 prior to the introduction of the washing step. Not knowing the exact composition of the Mn-LDH phase prevents a precise estimation of the diamagnetic contribution and does not allow quantitative evaluation of the magnetocaloric properties. The overall profile of the M-T curves suggests that antiferromagnetic ordering occurs at ~16 K. However, the ZFC and FC curves diverge below the transition temperature and neither exhibits a change in sign of the slope, thus it is likely that competing antiferromagnetic and ferromagnetic interactions are present, preventing the magnetic moments from aligning completely parallel or antiparallel. This is likely a consequence of the ferromagnetic double exchange mechanism arising from the mixed-valent Mn cations or ferromagnetic superexchange between Mn^{3+} cations competing with the antiferromagnetic superexchange mechanism expected between Mn^{2+} cations via -OH anions.

A linear fit to the inverse susceptibility versus temperature yields a Weiss temperature of -56 K, which indicates that moderate antiferromagnetic interactions dominate in the material. As such, the in-plane and interlayer interactions are both antiferromagnetic in nature.

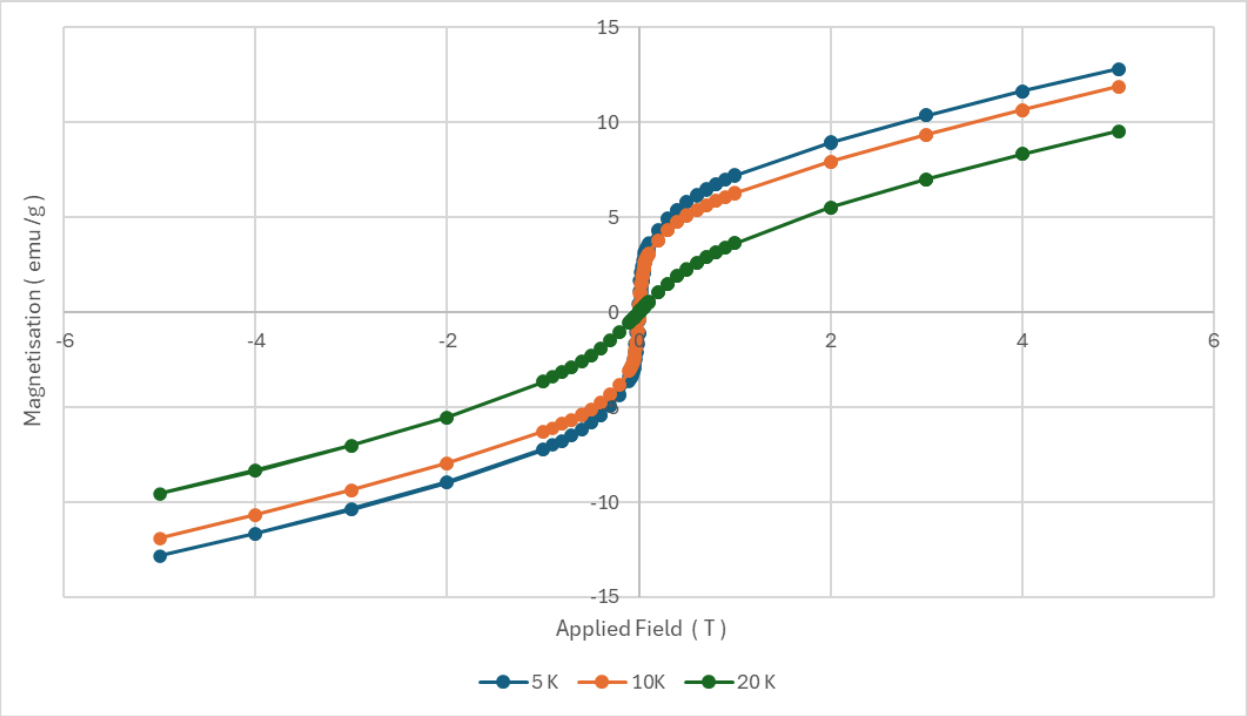

Figure 14: M-H of a mixture of Mn-LDH-1, Mn-LDH-2 and trace manganite

Magnetisation versus field (M-H) measurements were conducted from - 5 T to + 5 T at three different temperatures, below and above the transition temperature at 10 K and 20 K respectively, and at 5 K to minimize the impact of thermal effects on the magnetic ordering. The features of the data presented in figure 14 that are immediately apparent are that a ferromagnetic component is present with negligible remanent magnetisation and coercivity at all three temperatures. Low coercive fields are a desirable trait for magnetocaloric applications, allowing for faster cycling of the material and improving its performance in refrigeration devices. However, refrigeration devices rely on materials with high maximum cooling power that have large magnetic entropy changes in response to an applied field. The relatively low remanent and saturation magnetisation in this material indicate a smaller change in magnetic entropy and thus, a lower maximum cooling power making this material less suitable for magnetic refrigeration.

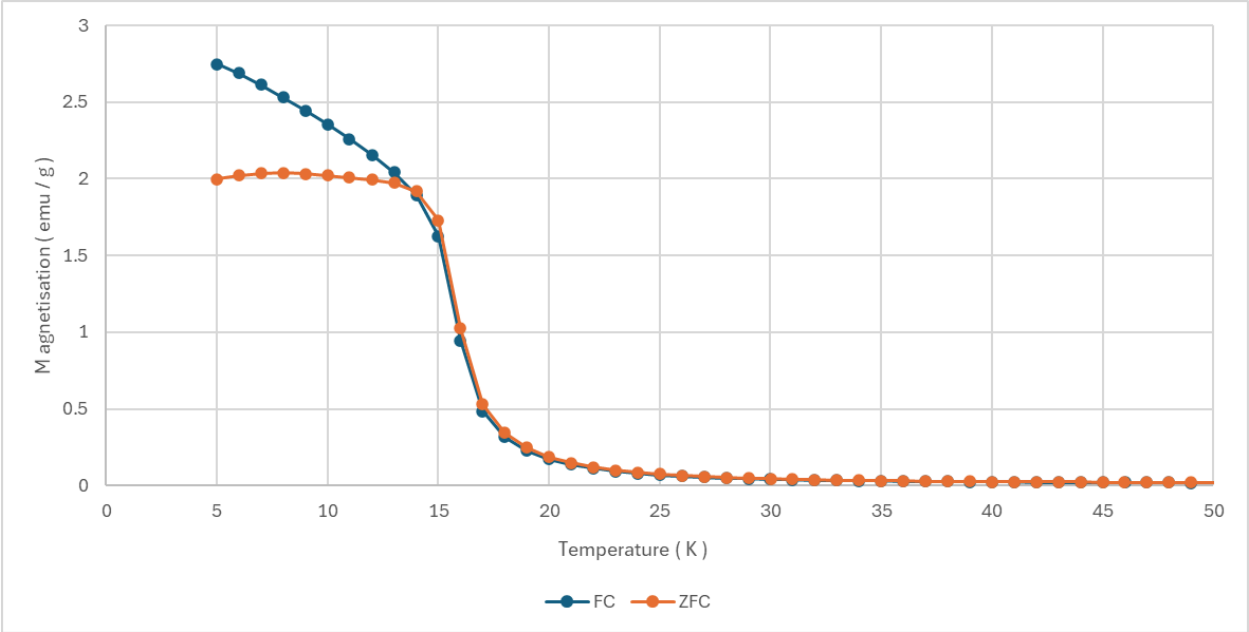

Figure 15: ZFC/FC M-T data for acid washed product (LDH-2)

In order to assess the effectiveness of the washing step and to compare the properties of the Mn-LDH-1 and Mn-LDH-2 phases, a M-T scan was performed on the sample from Batch 3 that was dried after washing and contained only Mn-LDH-2. The measurement was performed from 5 K to 200 K with an applied field of 0.1 T. The overall shape of the graph is similar to that in Figure 13, implying antiferromagnetic ordering with a ferromagnetic component (canted antiferromagnetism). Another explanation could be that the magnetic moments are geometrically frustrated due to the triangular lattice, preventing the magnetic moments from being completely parallel.

The Néel temperatures of the samples prior to and post-washing are similar, at 15 K and 16 K respectively. The inverse susceptibility versus temperature plot corresponding to the data in Figure 15 was obtained in the same manner as discussed before, yielding a Weiss temperature of -53 K indicating antiferromagnetic interactions with strength comparable to that of the unwashed product (-56 K). As such, the interlayer magnetic interactions in both Mn-LDH-1 and Mn-LDH-2 are likely a result of superexchange dominating over double exchange.

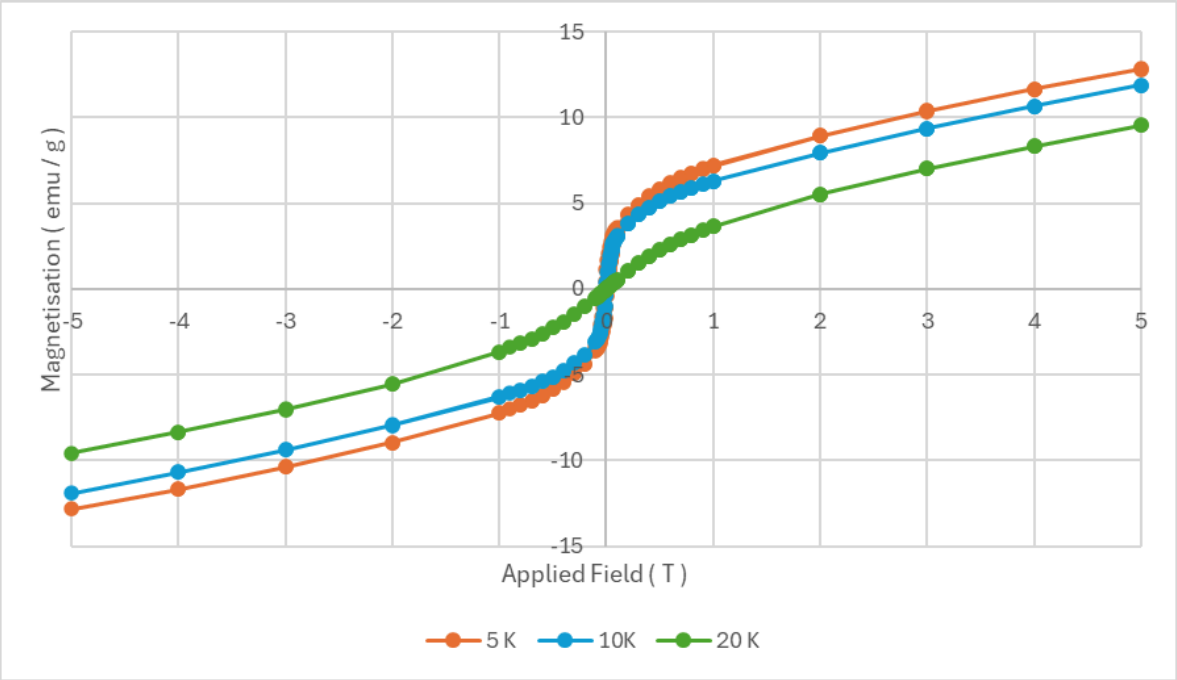

Figure 16: M-H data of compound washed with H_2SO_4

The material obtained after washing shows a narrow hysteresis loop with a low coercivity of 200 Oe at 5 K. Washing with sulfuric acid thus leaves a compound exhibiting soft magnetism. The M-H data follows the same shape as the unwashed sample, backing up the findings from M-T data.

Comparing the M-T curves for the samples prior to and post washing there is little difference in a magnetic susceptibility. Given the results, it could be that the phase remnant after washing exhibits higher magnetisation than the phase that is removed. In spite of this, since Neel and Weiss temperatures for both samples are comparable, it is more likely that washing the product with sulfuric acid has reduced the relative amount of non magnetic impurities to the product phases in the sample improving the magnetisation per gram as a larger portion of the product is magnetic.

3.2 Air stable Green Rust

Synthesis. Having chosen this compound for its stability to decomposition in air, the first batch of green rust was collected from the Pol-Eko furnace as a dark green viscous solution which was washed with ethanol, twice with a 1:1 mixture of ethanol and water, and lastly once more with ethanol. Leaving the product to dry on a heating plate at 100 °C for a week resulted in little evaporation, leading to the product being transferred to a vacuum oven and dried at 100 °C for another week yielding a fine green powder. Despite glycerol being used in the synthesis to improve the stability of green rust in air, the product visibly begins to absorb moisture from air within an hour of being exposed. Since the product remains in its dehydrated state when heated, this highlights the instability of the product in both the hydrated and anhydrous phases.

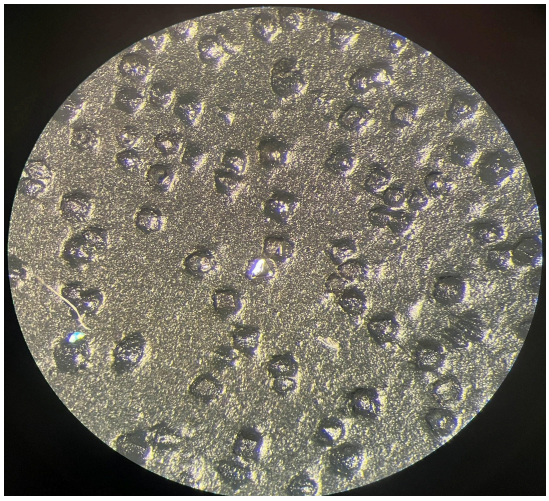

Figure 17: Green Rust product with impurity crystals

Drying the wet product in the vacuum oven overnight returned the sample to the original state obtained after washing and drying, implying that the moisture absorption by the product is partially reversible.

The difficulty of solvent evaporation and poor air stability suggest that a significant portion of glycerol remains in the sample, preventing the intercalation of lactate anions due to a glycerol coating. The time spent in the furnace was thus increased to achieve better crystallinity and, additionally, the amount of solvent used for washing was doubled to improve the purity of the product. Once washed, the product obtained was of the same color as the previous batch. However, the product became visibly dry after two days in the vacuum oven, in contrast to the two weeks it took initially. Furthermore, the product showed better stability, beginning to visibly absorb moisture only after one day of being exposed to open air.

3.2.1 Structural investigations. X-Ray Diffraction

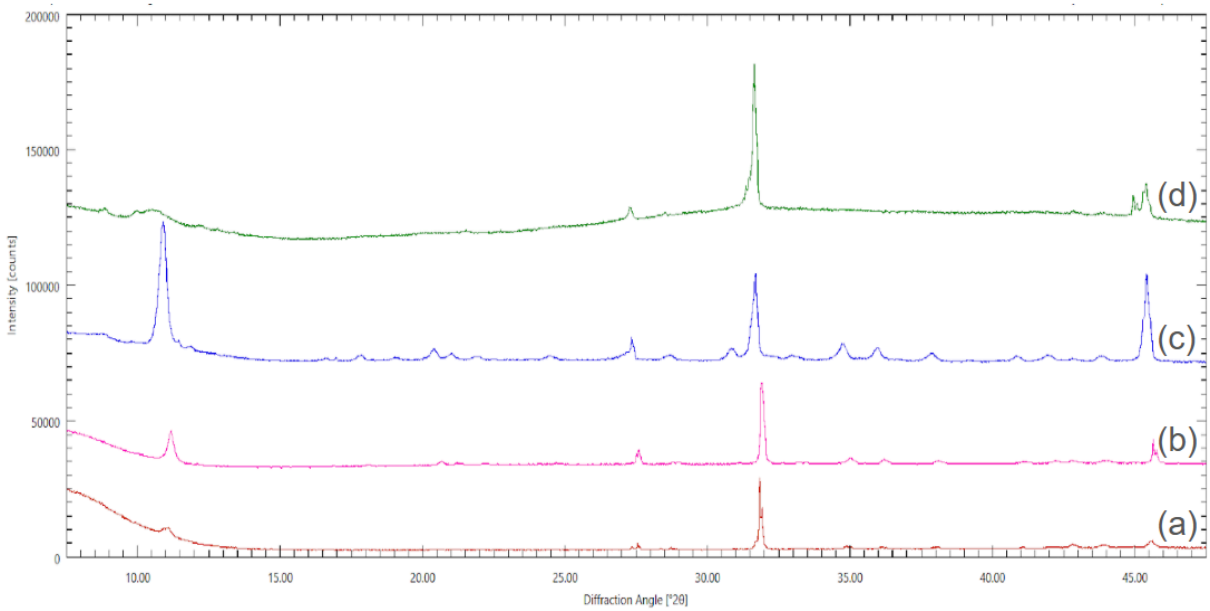

Figure 18: X-Ray Diffraction patterns for (a) Batch 1, unwashed; (b) Batch 1, washed with PropOH; (c) Batch 1, washed with EtOH / H_2O; (d) Batch 2, solvent evaporation, washed with EtOH

To investigate the effectiveness of the procedure and the effect of washing on the structure, four powder XRD measurements were conducted in the range 5-55 degrees 2Θ.

By comparing diffraction patterns (a)-(c) in Figure 18, it is apparent that washing the material does not cause the material to decompose as the characteristic 003 peak of Green Rust at 10.69 degrees 2Θ is present in all samples measured. However, the peak corresponding to rocksalt (NaCl) at 31.63 2Θ is also present in all samples analysed, which suggests that either not enough solvent was used to wash away the impurities or that the solvents used are not suitable to completely purify this reaction mixture, especially since glycerol is a viscous liquid making it difficult for the ethanol and water mixture to effectively wash the product.

For (b), washed with propanol, the relative ratio between the GR peak and NaCl peaks has increased in comparison to the unwashed sample, which is in line with the expectation that NaCl should be soluble in organic solvents such as aliphatic alcohols. The decrease in intensity for a variety of impurity peaks at higher angles highlights the importance of washing the product to reduce the amount of impurities present. However, the air stability provided by the intercalated lactate anions is also combined with glycerol remaining in solution, which makes washing less effective as evidenced by remnant impurity peaks despite their loss in intensity.

Regarding diffraction pattern (d), it is apparent that using the solvent evaporation method it is possible to obtain the desired product, evidenced by the 002 peak at 10.69 degrees 2Θ, but this approach results in a extra phase at 9.96° 2Θ amongst which is a compound with a layer spacing of 8.8 Å, comparable to 8.2 Å of GR, implying that another layered material has been synthesised along with the target product, lowering the overall yield of the procedure.

Furthermore, the layer spacing of 8.2 Å, as obtained from 002 peak at 10.69 2Θ, is not large enough to promote the ferromagnetic dipole-dipole interaction between the layers while superexchange remains dominant promoting antiferromagnetic interactions. As a result, Green Rust is an antiferromagnet which in general tends to exhibit lower magnetic entropy changes, and thus lower relative cooling power hindering its potential in magnetic refrigeration..

3.2.2 Magnetometry results

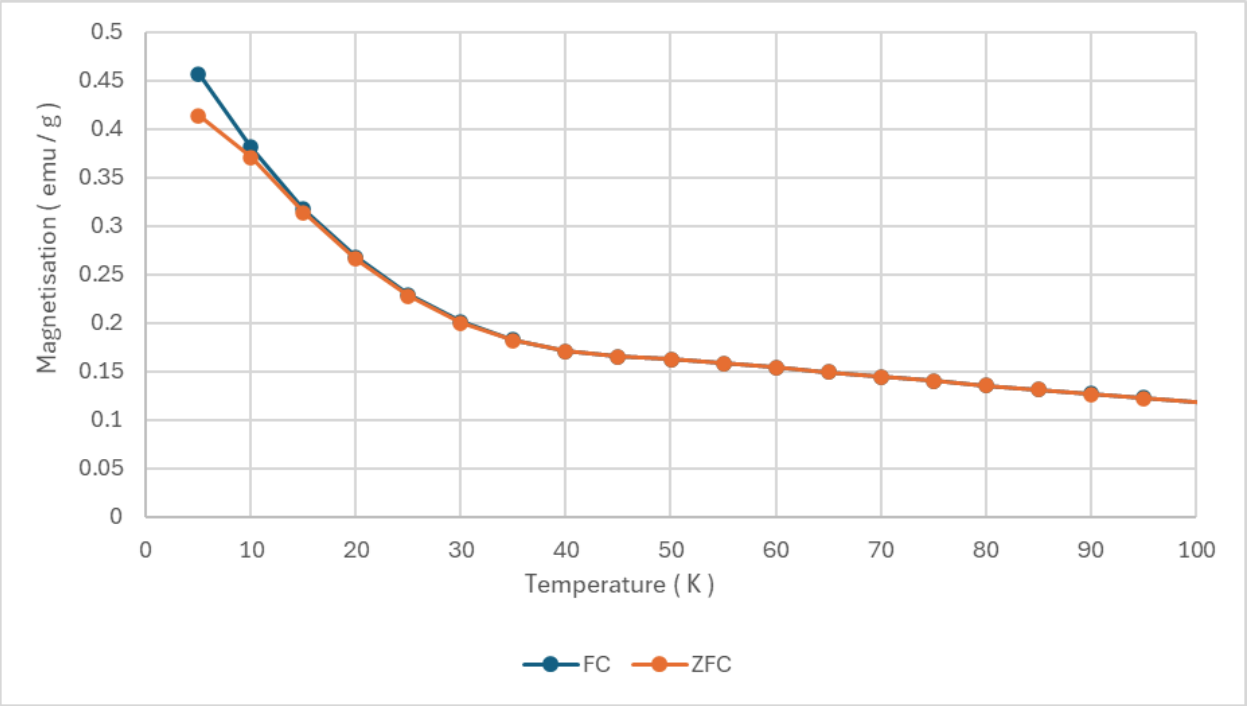

Figure 19: M-T data obtained for washed Green Rust

M-T scans were performed on the synthesised green rust on warming from 5 to 300 K with an applied field of 1000 Oe.

As seen in figure 19, the washed material exhibits largely paramagnetic behavior. A broad maximum at ~45 K suggests possible weak or short-range antiferromagnetic ordering. Following the same approach as for previous materials, AFM behaviour is evidenced by plotting the inverse susceptibility against temperature and extracting the Weiss temperature of -11.8 K. This is lower in magnitude than values found for the Mn-based LDH materials presented in this work, which have Weiss temperatures as low as -36 K indicative of stronger interactions. Negative Weiss temperatures point to the fact that in brucite-like layers of metal octahedra antiferromagnetic interactions dominate, likely driven by the superexchange mechanism.

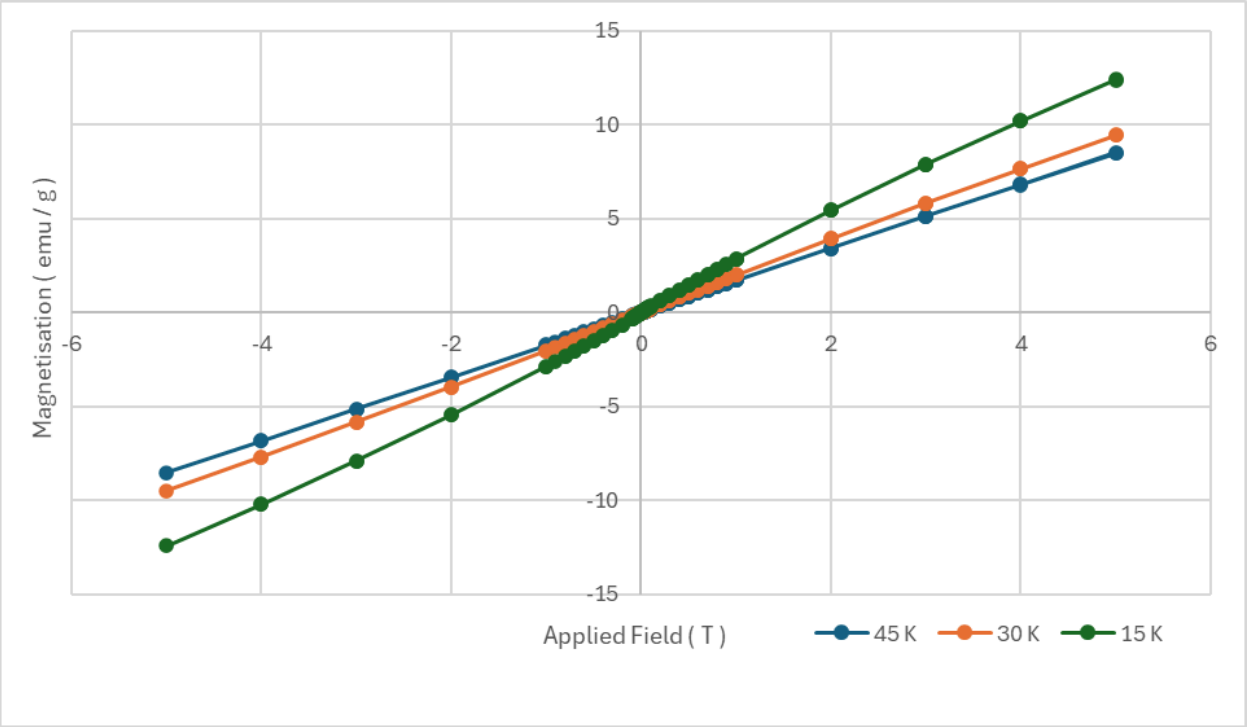

Figure 20: M-H data for unwashed Green Rust

The M-H data for the unwashed initial batch shows no hysteresis, but the curves are close to linear, implying purely antiferromagnetic interactions or paramagnetic spins, neither of which are promising for magnetocaloric applications despite the cyclability provided by negligible hysteresis. Taken together with the M-T data, it appears that this green rust sample exhibits only weak magnetic interactions and that much of the sample remains paramagnetic down to at least 5 K.

Without obtaining single crystals of air stable green rust, it is difficult to understand the influence of the crystal structure on θ_W, T_N and the magnetisation values; hence in-depth structural investigations would provide a better defined understanding of the product's morphology and what affects the resultant magnetic properties.

3.3 Air stable iron-based layered hydroxide

Figure 21: Photo of the product

Synthesis. Despite the lacking magnetic properties, intercalation of lactate anions proved to be an effective way to produce a stable layered metal hydroxide. As such, an iron-based layered hydroxide, different to Green Rust, was chosen in order to take advantage of increased stability and better magnetic properties. The product was collected as viscous suspension in glycerol. After drying for 48 hours in a vacuum oven the product was a dark green powder with an appearance much like the green rust synthesised in section 3.2. Unlike GR however, the mixture tended to form agglomerates and was affected by electrostatics to a greater extent than GR when handling. Nonetheless, the product was easier to dry and handle in comparison to green rust. Furthermore, Fe-LSH still absorbs moisture gradually when left at room temperature in air but at a much slower rate than green rust which becomes visibly moist within an hour, whereas the appearance of Fe-LSH did not approach that of green rust even after a week of being in air.

3.3.1 Structural investigations. X-Ray Diffraction

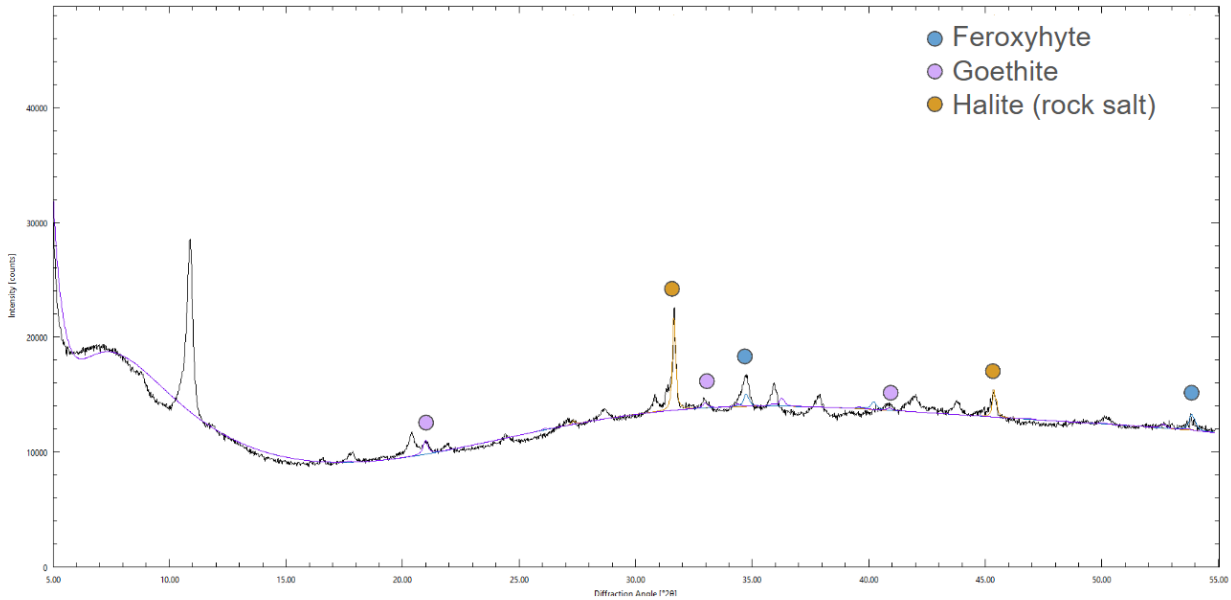

Figure 22: X-Ray Diffraction patterns of (a) Batch 1, 24h ; (b) Batch 2, 48 h and reduction with hydrogen

The XRD pattern shows a variety of peaks. Running a Rietveld fit to the data suggests the presence of feroxyhyte (δ-FeO(OH)), goethite (α-FeO(OH)) and halite (NaCl) as demonstrated in figure 22. The relatively intense peak at 11.4 degrees 2Θ is likely caused by the target product and is at the position close to that of 003 peak of Green Rust indicating an inter-layer spacing of 8.1 Å, comparable to that of Green Rust (8.2 Å).

After attempted reduction with 5% hydrogen gas in argon at 100 °C for 24 hours, all of the peaks attributed to Fe-LSH prior to reduction are still present, implying that the temperature and time chosen were too low to result in successful reduction of a sizable portion of Fe^{3+} metal centers.

3.3.2 Magnetometry.

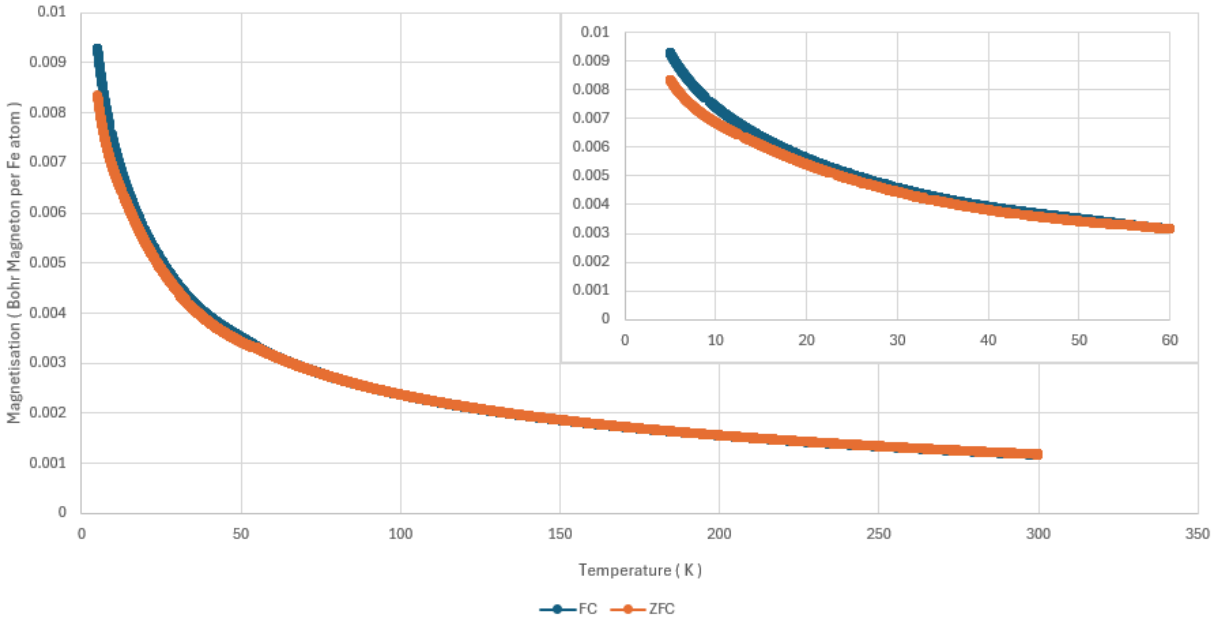

Figure 23: M-T ZFC/FC data of Fe-based layered simple hydroxide

M-T data were collected on the sample that had undergone attempted reduction, and analysis yielded an effective magnetic moment of 3.95 μ_B per Fe atom, which is indicative of the iron centers being primarily in the 2+ oxidation state. Specifically, the ratio of Fe^{2+} to Fe^{3+} was found to be 1:31 which implies the system is dominated by superexchange between adjacent Fe^{3+} cations. The M-T data exhibit a weak anomaly and divergence of the FC and ZFC curves at ~45 K with a Weiss temperature of -101 K, suggesting that the in-plane antiferromagnetic interactions are the strongest investigated in this work. M-H curves were measured and the magnetic entropy change was calculated as a function of temperature, yielding 1.19 J / kg.K at 7 K.

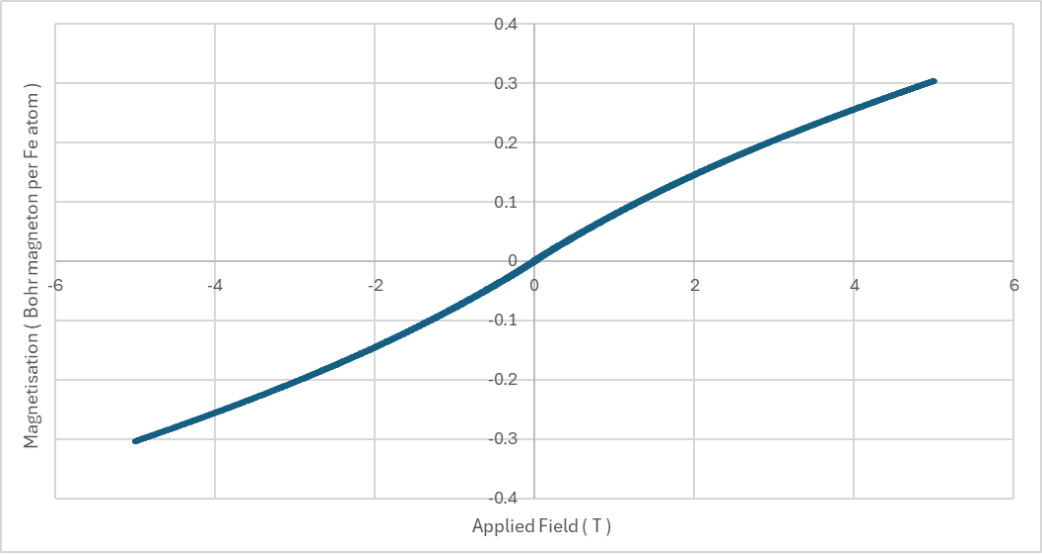

Figure 24: M-H data of Fe-LSH from - 5 T to + 5 T at 5 K\

Fe-LSH exhibits largely paramagnetic behaviour down to 5 K, perhaps due to the presence of disorder which prevents long-range magnetic order. While the low saturation magnetization of 0.3 μ_B per iron atom in a field of 5 T is not promising for magnetocaloric applications, the low coercivity allows for high cyclability of the system.

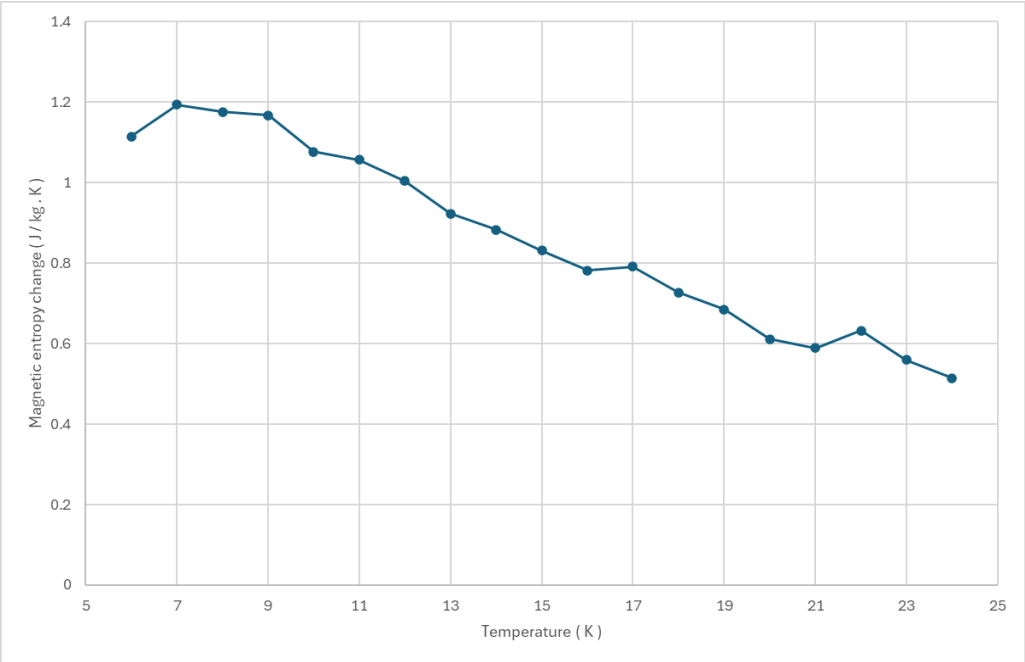

Figure 25: ΔS_{Mag} - T data for Fe-LSH

Using equation (7), the maximum magnetic entropy change was calculated to be 1.19 J / kg.K at 5 T which is considerably lower than rare-earth alternatives, such as holmium diboride with 40.1 J / kg.K at 5 T. The calculation of relative cooling power is not warranted given the shape of the graph.

3.4 Cobalt-based layered double hydroxide $Co_5 (OH)_6 (SeO_4)_2$ 4 H_2O

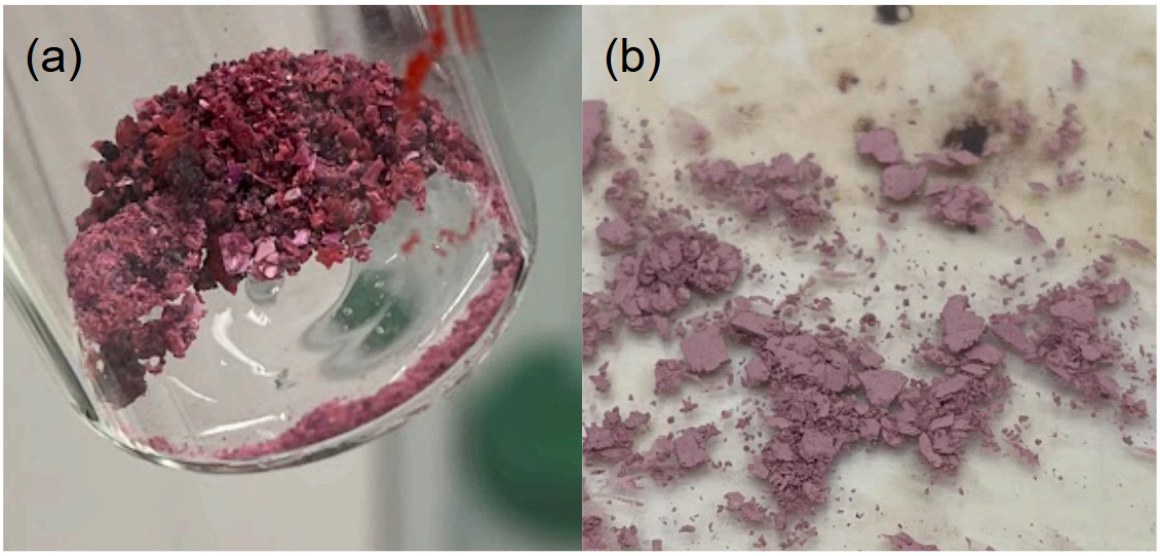

Figure 26: Product photos of (a) cobalt selenate pentahydrate and (b) $Co_5 (OH)_6 (SeO_4)_2 \cdot 4 H_2O$

Synthesis. Cobalt-based layered double hydroxide, chosen for its ferromagnetic behaviour and air stability, was prepared in a two-step process. During the first step of the synthesis procedure, cobalt selenate was obtained as pink crystals via evaporation of water at 80 °C for two days. Once dried, the cobalt selenate crystals were weighed out and crushed for the second step of the procedure. Notably, the coarse crystals of cobalt selenate need to be crushed thoroughly to avoid dissolution taking more than one day which would give trace amounts of oxygen time to oxidise Co^{2+} present in solution. The degree of oxidation becomes apparent when NaOH is added to solution, resulting in a nearly immediate change of color indicative of LDH formation. In contrast to the literature, the suspension turned purple rather than blue which could indicate that a different major product is formed.[27]

The resultant suspension was hydrothermally treated at 150 °C for 24 hours yielding a mixture with two distinct phases: a clear red water layer and viscous pink product layer. The former was decanted and the latter was transferred to a funnel where it was washed with acetone, ethanol and water yielding a pink powder which was completely dried after 15 min at 40 °C on a heating plate in air.

3.4.1 XRD

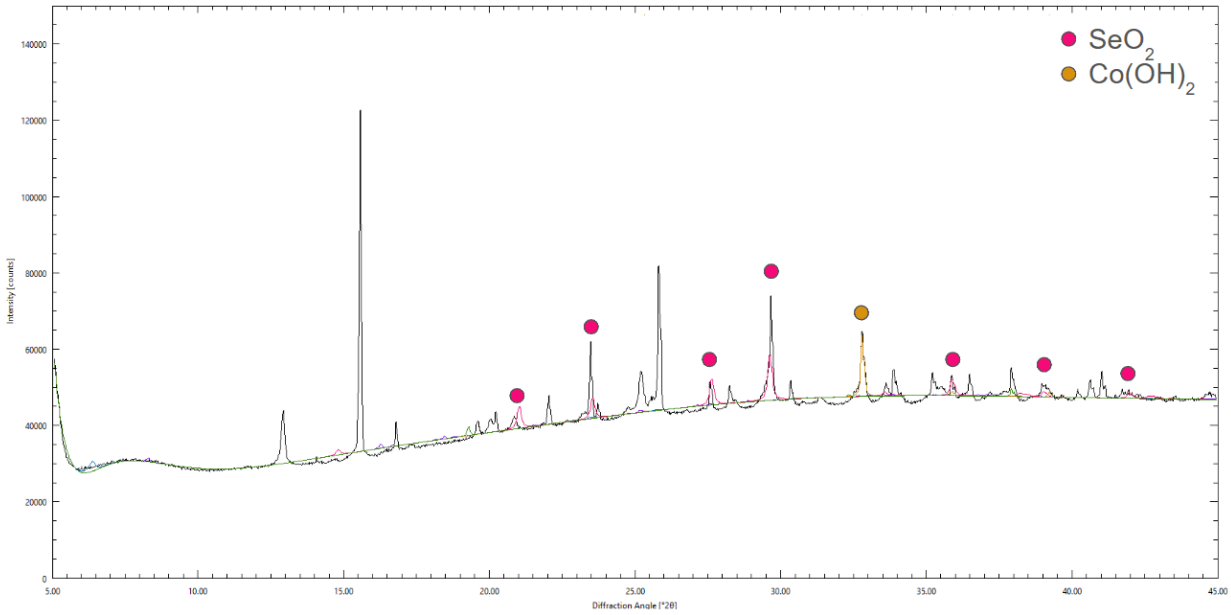

Figure 27: Powder X-Ray Diffraction pattern of Batch 2, performed entirely under nitrogen

The powder XRD scan was conducted following the same protocol as for the rest of the measurements described thus far. Comparing the pattern obtained with that given in the literature, the peaks at 15.4 degrees 2Θ and 16.7 degrees 2Θ match those in the original paper. However, the 00l peak from the literature report is absent and a new peak is present at 12.8 degrees 2Θ which corresponds to a lattice parameter of 13.8 Å under the assumption that this is the 002 peak, which is much smaller than the reported lattice parameter of 21.4 Å. While this spacing is plausible for a layered system, the disparity suggests that the interlayer structure is different to that of the target material. The peaks labeled in figure 27 are attributed to SeO_2 and $Co(OH)_2$ whose presence would suggest that selenate and cobalt octahedra

were not fully incorporated in the structure. The smaller spacing between the brucite-like layers of cobalt hydroxide octahedra implies inter-layer antiferromagnetic interactions.

3.4.2 Magnetometry

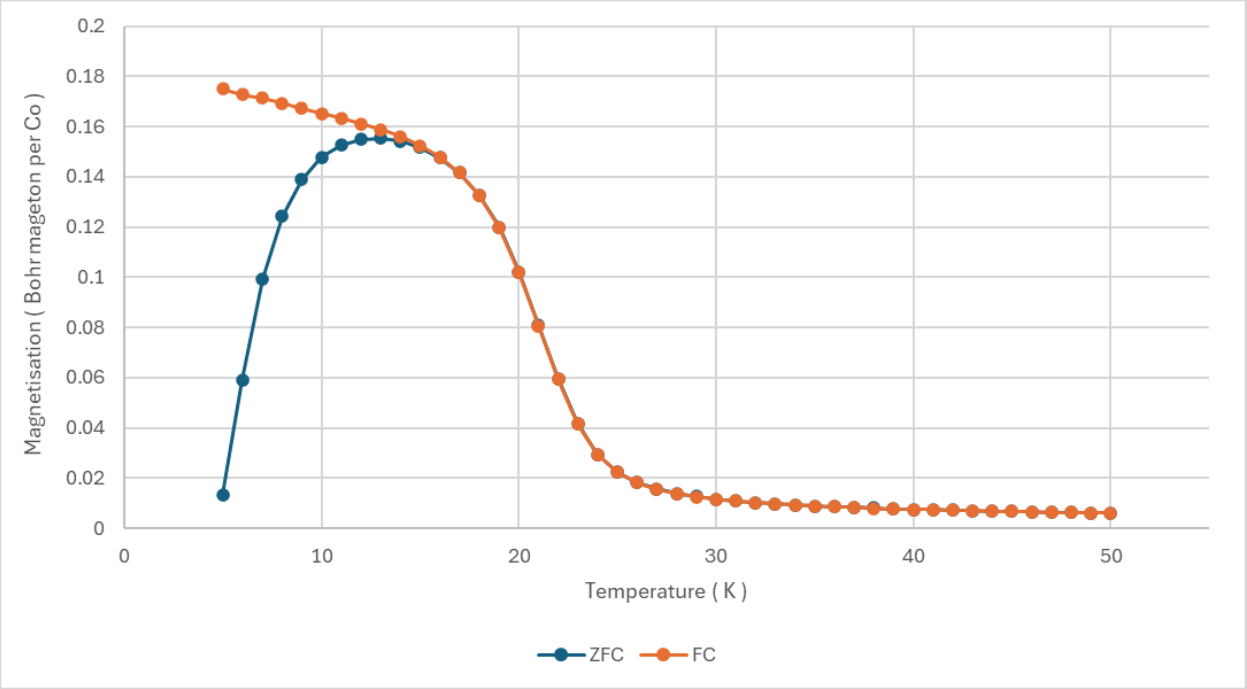

Figure 28: Comparison between ZFC and FC measurements for $Co_5(OH)_6(SeO_4)_2$ 4 H_2O AT 0.1 T from 5 to 50 K

Once synthesised and dried, the product was analysed following the ZFC/FC procedure with an applied field of 0.1 T. As seen in figure 28, the overall profile of the graph suggests antiferromagnetic behavior as evidenced by the gradual decrease in slope with decrease in temperature for the ZFC curve below the transition temperature. The divergence between the ZFC heating and FC heating curves implies that even at the lowest temperatures, there is a degree of disorder in the system hindering the ability of the magnetic moments to align in completely antiparallel fashion below the Néel temperature of 20 K. The Weiss temperature, found to be -16 K, indicates antiferromagnetic interactions that are weaker than those found for the investigated Mn-LDH-1, Mn-LDH-2 and Fe-LSH.

The effective magnetic moment was calculated from the Curie constant to be 3.95 μ_B per Co atom implying that the majority of cobalt cations are in the 2+ oxidation state. Using equation 6, the ratio of Co^{2+} to Co^{3+} was found to be 11.50:1. As such, the inlayer interactions are dominated by superexchange rather than double exchange. Since the majority of cations present are Co^{2+}, the superexchange is in nature similar to $Fe(OH)_2$ where the inlayer interactions are ferromagnetic. However, the magnetic behaviour of the material is antiferromagnetic because of the layer spacing promoting antiferromagnetic arrangement of the layers.

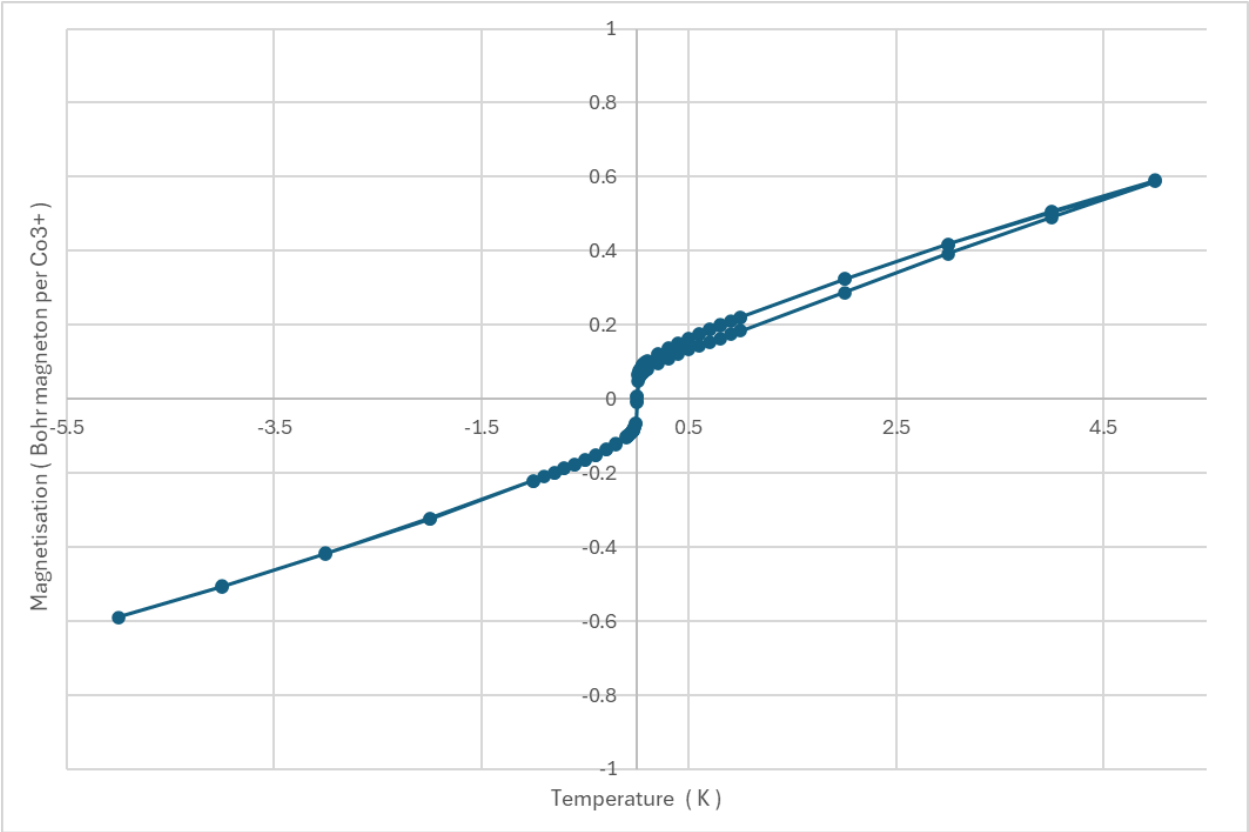

Figure 29: M-H data recorded at 20 K from - 5 T to + 5 T for $Co_5(OH)_6(SeO_4)_2$ 4 H_2O

The M-H data, shown in figure 29, indicates that $Co_5(OH)_6(SeO_4)_2$ $4H_2O$ exhibits a small ferromagnetic moment with no magnetic hysteresis. While this allows for fast cycling of the magnetisation, the saturation magnetisation of only 0.6 μ_B per Co at 5 T implies poorer magnetocaloric performance than in similar ferromagnetic systems exhibiting low coercivity.

3.5 $Na_2Mn(SO_4)_2 \cdot 2\,H_2O$ crystals. Magnetometry

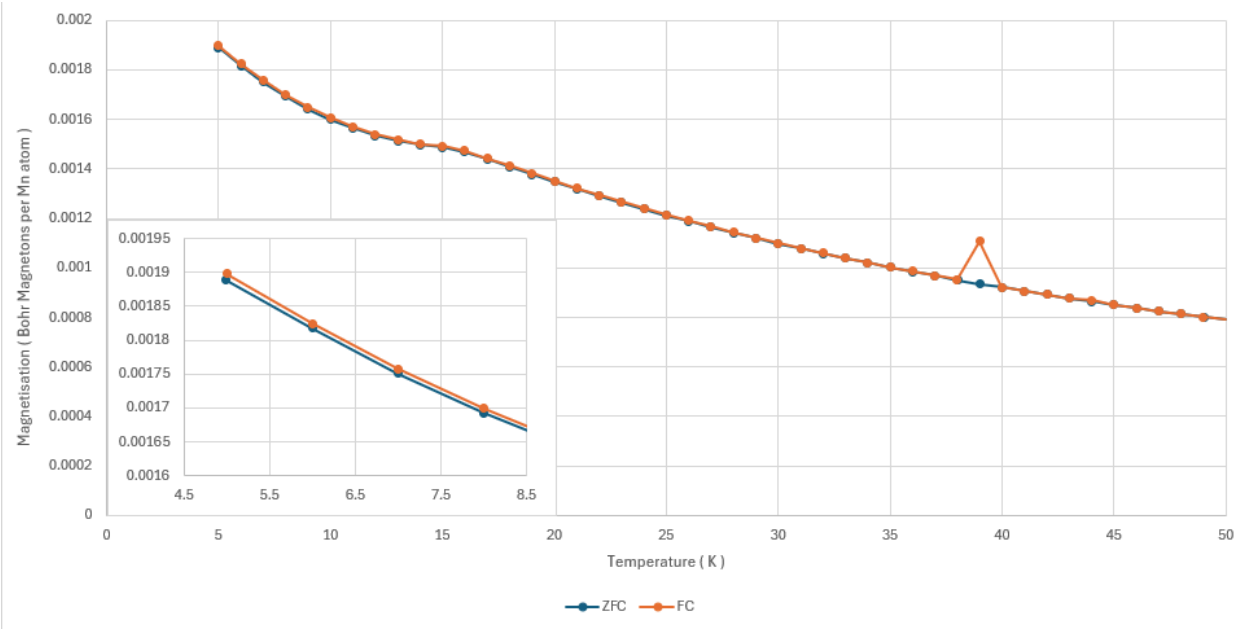

Figure 30: M-T ZFC/FC data with applied field of 0.01 T from 5 to 50 K for $Na_2Mn(SO_4)_2{\cdot}2H_2O$

Having obtained and identified crystals of $Na_2Mn(SO_4)_2{\cdot}2H_2O$, M-T scans were conducted on the product to determine the viability of the synthesised material for magnetocaloric applications despite it not being a layered system. There is a subtle bump at around 14 K that could indicate an antiferromagnetic transition. However, the increase in slope below the transition temperature suggests that the material remains largely paramagnetic. In other words, as the temperature is lowered, antiferromagnetic ordering begins to set in but there is possible disorder preventing completely antiparallel alignment of the magnetic moments, meaning that long range order is suppressed.

The Weiss temperature was obtained from a linear fit to the inverse susceptibility versus temperature plot using the same methodology as for previous experiments. The Weiss temperature was found to be -18 K, indicative of antiferromagnetic interactions of comparatively lower strength than previous samples.

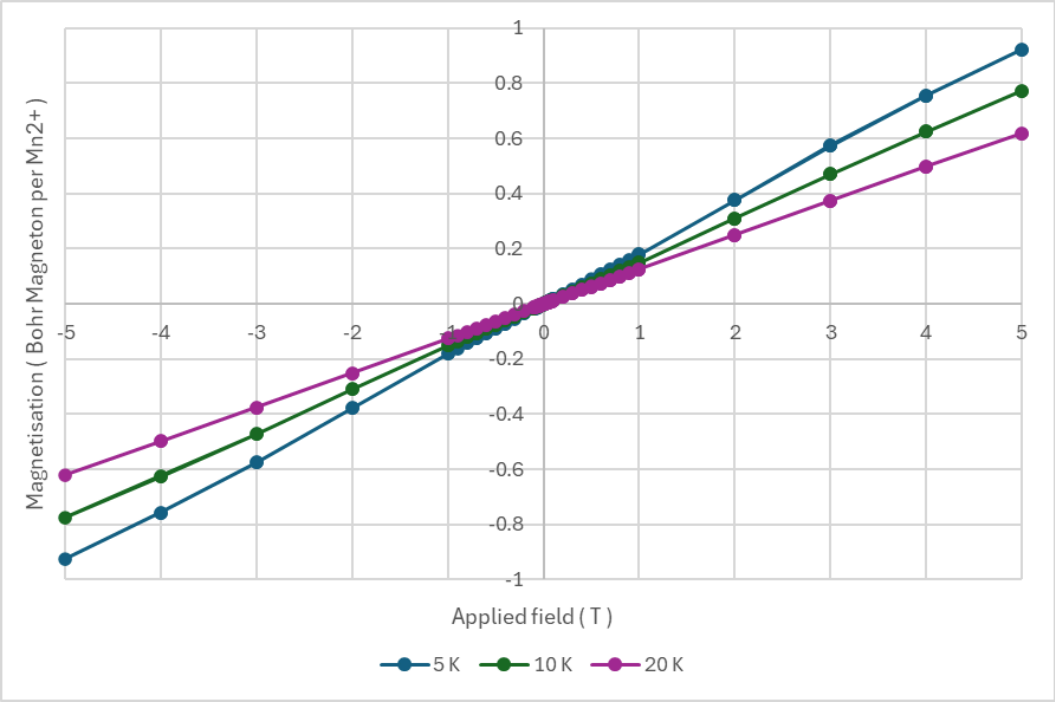

Figure 31: M-H data for crystals of $Na_2Mn(SO_4)_2$ 2 H_2O from -5 to + 5 T at 5 K, 10 K, 20 K

Crystals of $Na_2Mn(SO_4)_2{\cdot}2H_2O$ exhibit low coercivity of less than 100 Oe at 5 K making them soft magnets which is desirable for MCE applications. Despite this, similarly to the previous samples the crystals lack any notable ferromagnetic contribution down to 5 K, which results in a low magnetic entropy change and thus a lower maximum cooling power. $Na_2Mn(SO_4)_2{\cdot}2H_2O$ is thus likely to be an antiferromagnet with only short-range order such that the M-H profile resembles that of a paramagnet. Given the results obtained, this material is unsuitable for magnetic refrigeration via the magnetocaloric effect.

Conclusion

This research focuses on investigating the synthesis, structure, and magnetic properties of monometallic layered metal hydroxides. Synthesised via solvent evaporation, an air sensitive mixture of two compositions of manganese-based layered hydroxides was obtained along with manganite and non-magnetic impurities. While the lack of single crystals prevents full structure determination, washing the product with 1 % sulfuric acid improves the purity of the final mixture. The M-T curves of both compositions, labeled Mn-LDH-1 and Mn-LDH-2, reveal antiferromagnetic ordering with Weiss temperatures of -56 K and -53 K respectively. Mn-LDH-1 and Mn-LDH-2 undergo a magnetic transition with Néel temperatures of 15 K and 16 K. The M-H data reveal both compositions to be soft magnets with low saturation magnetisation of 0.20 emu / g and 0.51 emu /g at 5 Tesla respectively.

Synthesised via solvothermal treatment, an air-stable variant of green rust, $[Fe^{II}_{0.33}Fe^{III}_{5.67}(OH)_{12}]$ $3[C_3H_5O_3]$ • $1.33[CO_3]$, was synthesised from iron chloride hexahydrate and sodium acetate in glycerol; additionally yielding magnetite and rocksalt as side products. While intercalated lactate anions improved the air stability of the product, washing with ethanol and water proved to be essential to obtaining a

product that does not absorb moisture from the air. The M-T profile of the green rust points to a magnetic transition at 45 K with a Weiss temperature of -36 K, indicative of antiferromagnetic behaviour. The M-H profile indicates that the system is unable to establish complete antiparallel alignment of the spins leading to behaviour that is largely paramagnetic in nature with the saturation magnetisation being 12 emu / g at 5 Tesla.

Utilising the lactate anions to improve air stability, an iron-based layered simple hydroxide was synthesised from iron sulfate heptahydrate and sodium hydroxide in glycerol yielding a dark green powder that is stable in air. The effective magnetic moment of 3.95 μ_B is indicative of Fe(II) being the dominant oxidation state; the ratio Fe^{2+}:Fe^{3+} was found to be 31:1. The compound undergoes an antiferromagnetic transition at 45 K with a Weiss temperature of -101 K, implying strong interactions, probably involving superexchange. The magnetic entropy change is 1.19 J / kg.K at 7 K which despite being lower than currently used rare-earth alternatives, offers a more sustainable solution to magnetic refrigeration.

Having failed to successfully synthesize $Co_5(OH)_6(SeO_4)2{\cdot}4H_2O$, it became apparent that a structure containing cobalt hydroxide octahedra between the brucite-like layers likely formed. While the lattice spacing suggests that some anions were intercalated between the layers, such as selenates, the interlayer spacing is not large enough to promote ferromagnetic interactions between the layers, letting the layers couple antiferromagnetically. Despite this, the ratio of Co^{2+} to Co^{3+} cations suggests ferromagnetic superexchange dominates in the layer. The material exhibits an antiferromagnetic transition at 20 K with a weak ferromagnetic component, reaching a saturation magnetisation of 0.6 μ_B per cobalt atom at 5 Tesla. Overall, $Co_5(OH)_6(SeO_4)2{\cdot}4H_2O$ is the most suitable for hydrogen liquefaction out the compounds examined in this work.

A non-layered compound was obtained in the form of single crystals during the investigation of manganese-based layered double hydroxides, which prompted further study of the material. The crystals of $Na_2Mn(SO_4)_2{\cdot}2H_2O$ were obtained by the evaporation of water, and subsequent washing and recrystallizing with ~1% sulfuric acid in air. The product was obtained as black crystals exhibiting antiferromagnetic behaviour with a Weiss temperature of -12 K.

Overall, layered metal hydroxides present a promising alternative to rare-earth based materials used in hydrogen liquefaction because of the tunability of their properties. Tuning the layer spacing is integral to promote ferromagnetic coupling between the layers, increasing the remanent and saturation magnetization thereby increasing the magnetic entropy change. Additionally, as demonstrated with lactate anions, tactical intercalation of certain molecules protects the metal centers from oxidation via exposure to air. The choice of metal is crucial to promoting either double exchange within the layer, resulting in ferromagnetic ordering within the layers, or in some cases ferromagnetic superexchange. As such, while layered metal hydroxides are promising candidates for hydrogen liquefaction, they require further optimisation and investigation of synthesis procedures, oxidation kinetics and the balance between competing magnetic interactions in order to improve the magnetic entropy change, air stability and cyclability.

Bibliography

1. Aziz, M. Liquid Hydrogen: A Review on Liquefaction, Storage, Transportation, and Safety. Energies 2021, 14 (18), 5917. DOI:10.3390/en14185917.

2. Pankratov, N. Yu.; Tereshina, I. S.; Nikitin, S. A. Magnetocaloric Effect in Rare-Earth Magnets. *Physics of Metals and Metallography* **2023**, *124* (11), 1139–1146. DOI:10.1134/s0031918x23601841.

3. Santos, J. P.; Morais, R. H. M.; Francisco, R. M.; Rosa, D. S.; Nepomuceno, E. Magnetocaloric Effect Properties in the Ashkin–Teller Model. *Journal of Magnetism and Magnetic Materials* **2024**, *607*, 172407. DOI:10.1016/j.jmmm.2024.172407.

4. Aliev, A. M.; Gamzatov, A. G. Magnetocaloric Effect in Manganites in Alternating Magnetic Fields. *Journal of Magnetism and Magnetic Materials* **2022**, *553*, 169300. DOI:10.1016/j.jmmm.2022.169300.

5. Aliev, A. M.; Gamzatov, A. G. Magnetocaloric Effect in Alternating Magnetic Fields: A Review. *Physics of Metals and Metallography* **2024**, *125* (14), 1901–1926. DOI:10.1134/s0031918x24602518.

6. Materials, F. Magnetocalorics. https://www.mawi.tu-darmstadt.de/fm/research_fm/research_topics_fm/magnetocaloric_materials_fm/index.en.jsp (accessed 2025-07-08).

7. Castro, P. B.; Terashima, K.; Yamamoto, T. D.; Hou, Z.; Iwasaki, S.; Matsumoto, R.; Adachi, S.; Saito, Y.; Song, P.; Takeya, H.; Takano, Y. Machine-Learning-Guided Discovery of the Gigantic Magnetocaloric Effect in Hob2 near the Hydrogen Liquefaction Temperature. *NPG Asia Materials* **2020**, *12* (1). DOI:10.1038/s41427-020-0214-y.

8. Castro, P. B.; Terashima, K.; Yamamoto, T. D.; Iwasaki, S.; Matsumoto, R.; Adachi, S.; Saito, Y.; Takeya, H.; Takano, Y. Effect of Dy Substitution in the Giant Magnetocaloric Properties of Hob2. *Science and Technology of Advanced Materials* **2020**, *21* (1), 849–855. DOI:10.1080/14686996.2020.1856629.

9. Tajat, N.; El Hayaoui, W.; Bougdour, N.; Idlahcen, A.; Radaa, C.; Bakas, I.; Tamimi, M.; Cherkaoui, O.; Badreddine, M.; Assabbane, A.; Qourzal, S. Utilization of Zn–al–Cl Layered Double Hydroxide as an Adsorbent for the Removal of Anionic Dye Remazol Red 23 in Aqueous Solutions: Kinetic, Equilibrium, and Thermodynamic Studies. Nanotechnology for Environmental Engineering 2022, 7 (2), 343–357. DOI:10.1007/s41204-022-00237-1.

10. Miyamoto, H. The Magnetic Properties of Fe(OH)2. Materials Research Bulletin 1976, 11 (3), 329–335. DOI:10.1016/0025-5408(76)90199-9.

11. Farshidfar, F.; Lapolla, M.; Fattahi, A.; Ghandi, K. On the Structural and Electrical Properties of MGFE2O4, MGMN0.2Fe1.8O4, and MN3O4. *Heliyon* **2023**, *9* (11). DOI:10.1016/j.heliyon.2023.e21677.

12. Topping, C. V.; Kirschner, F. K.; Blundell, S. J.; Baker, P. J.; Woodruff, D. N.; Schild, F.; Sun, H.; Clarke, S. J. Coexistence of Magnetism and Superconductivity in Separate Layers of the Iron-Based Superconductor Li1−xFex(OH)Fe1−ySe. *Physical Review B* **2017**, *95* (13). DOI:10.1103/physrevb.95.134419.

13. Patil, D. S.; Pawar, S. A.; Kim, H. J.; Shin, J. C. Hierarchical Manganese–Iron-Layered Double Hydroxide Nanosheets for Asymmetric Supercapacitors. *Energies* **2020**, *13* (18), 4616. DOI:10.3390/en13184616.

14. Huang, T.; Pan, L.; Dong, J.; Zhou, L.; Tao, H.; Zhang, S.; Li, A. A Comprehensive Investigation of Zeolite-Rich Tuff Functionalized with 3-Mercaptopropionic Acid Intercalated Green Rust for the Efficient Removal of Hgii and Crvi in a Binary System. *Journal of Environmental Management* **2022**, *324*, 116344. DOI:10.1016/j.jenvman.2022.116344.

15. Perez, J. P.; Mangayayam, M. C.; Rubio, S. N.; Freeman, H. M.; Tobler, D. J.; Benning, L. G. Intercalation of Aromatic Sulfonates in 'Green Rust' via Ion Exchange. *Energy Procedia* **2018**, *146*, 179–187. DOI:10.1016/j.egypro.2018.07.023.

16. Huang, T.; Su, Z.; Dai, Y.; Zhou, L. Enhancement of the Heterogeneous Adsorption and Incorporation of Uraniumvi Caused by the Intercalation of β-Cyclodextrin into the Green Rust. *Environmental Pollution* **2021**, *290*, 118002. DOI:10.1016/j.envpol.2021.118002.

17. Cornu, D.; Coustel, R.; Durand, P.; Carteret, C.; Ruby, C. How Can Ph Drop While Adding NaOH? Formation and Transformation of MN4(OH)6SO4. *Journal of Solid State Chemistry* **2022**, *305*, 122631. DOI:10.1016/j.jssc.2021.122631.

18. Mamun, A. A.; Onoguchi, A.; Granata, G.; Tokoro, C. Role of Ph in Green Rust Preparation and Chromate Removal from Water. *Applied Clay Science* **2018**, *165*, 205–213. DOI:10.1016/j.clay.2018.08.022.

19. Zhang, Q.; Li, M.; Kong, J.; Chen, Y.; Liu, J. Explanation and Exploration of the Isothermal Titration Curve for the NaCl + Na2SO4+ H2O System at 298.15 K and 102.2 KPA. *ACS Omega* **2022**, *7* (29), 25811–25821. DOI:10.1021/acsomega.2c03339.

20. Chen, H.; Cui, H.; Zhong, R.; Xie, Y.; Yu, C.; Li, Z.; Ling, Y. Solubility of NA2SO4 in Silica-Saturated Solutions: Implications for Ree Mineralization. *American Mineralogist* **2020**, *105* (11), 1686–1694. DOI:10.2138/am-2020-7470.

21. Voisin, T.; Erriguible, A.; Philippot, G.; Ballenghien, D.; Mateos, D.; Cansell, F.; Iversen, B. B.; Aymonier, C. Investigation of the Precipitation of NA2SO4 in Supercritical Water. *Chemical Engineering Science* **2017**, *174*, 268–276. DOI:10.1016/j.ces.2017.09.009.

22. Zaki, A. H.; Tsunoji, N.; Ide, Y. Controlled Synthesis of Oxidation-Insensitive Green Rust, a Mixed-Valent Iron Mineral, for Enhancing Solar Hydrogen Production via Hydrolysis of Ammonia Borane. *ACS Sustainable Chemistry & Engineering* **2023**, *11* (6), 2295–2302. DOI:10.1021/acssuschemeng.2c05862.

23. Tahawy, R.; Doustkhah, E.; Abdel-Aal, E.-S. A.; Esmat, M.; Farghaly, F. E.; El-Hosainy, H.; Tsunoji, N.; El-Hosiny, F. I.; Yamauchi, Y.; Assadi, M. H.; Ide, Y. Exceptionally Stable Green Rust, a Mixed-Valent Iron-Layered Double Hydroxide, as an Efficient Solar Photocatalyst for H2 Production from Ammonia Borane. *Applied Catalysis B: Environmental* **2021**, *286*, 119854. DOI:10.1016/j.apcatb.2020.119854.

24. Ounacer, M.; Coustel, R.; Cornu, D.; Ona-Nguema, G.; Besson, F.; Carteret, C.; Abdelmoula, M.; Ruby, C. The Role of Iron(Ii) Excess and Phosphate to Synthesize Hydroxychloride Green Rust. *Colloids and Surfaces A: Physicochemical and Engineering Aspects* **2024**, *703*, 135409. DOI:10.1016/j.colsurfa.2024.135409.

25. Kim, M.-S.; Kim, T.-H.; Seo, Y. S.; Oh, J.-M.; Park, J. K. A Novel Synthesis of an Fe3+/Fe2+ Layered Double Hydroxide ('Green Rust') via Controlled Electron Transfer with a Conducting Polymer. *Dalton Transactions* **2017**, *46* (24), 7656–7659. DOI:10.1039/c7dt00731k.

26. Usman, M.; Byrne, J. M.; Chaudhary, A.; Orsetti, S.; Hanna, K.; Ruby, C.; Kappler, A.; Haderlein, S. B. Magnetite and Green Rust: Synthesis, Properties, and Environmental Applications of Mixed-Valent Iron Minerals. *Chemical Reviews* **2018**, *118* (7), 3251–3304. DOI:10.1021/acs.chemrev.7b00224.

27. Maalej, W.; Vilminot, S.; André, G.; Kurmoo, M. Synthesis, Magnetic Structure, and Properties of a Layered Cobalt−hydroxide Ferromagnet, Co5(OH)6(SeO4)2(H2O)4. *Inorganic Chemistry* **2010**, *49* (6), 3019–3024. DOI:10.1021/ic9025552.

28. Altomare, A.; Cuocci, C.; Giacovazzo, C.; Moliterni, A.; Rizzi, R.; Corriero, N.; Falcicchio, A. *J. Appl. Crystallogr.* **2013**, *46*, 1231–1235.

29. Döbelin, N.; Kleeberg, R. Profex: a graphical user interface for the Rietveld refinement program BGMN. *J. Appl. Crystallogr.* **2015**, *48*, 1573–1580. https://doi.org/10.1107/S1600576715014685

30. Cornu, D.; Coustel, R.; Renaudin, G.; Rogez, G.; Renard, A.; Durand, P.; Carteret, C.; Ruby, C. Synthesis and Characterization of a New Monometallic Layered Double Hydroxide Using Manganese. *Dalton Transactions* **2022**, *51* (31), 11787–11796. DOI:10.1039/d2dt01835g.

31. Plyusnina, L. P.; Likhoidov, G. G.; Barinov, N. N. Mn(II) → Mn(Iii) Oxidation Kinetics and Its Effect on Crystallization of Nanodisperse Platinum at 200–300°C and 1 Kbar. *Russian Journal of Inorganic Chemistry* **2011**, *56* (9), 1358–1362. DOI:10.1134/s003602361109018x.

32. Wildner, M.; Stoilova, D. Crystal Structures and Crystal Chemical Relationships of Kröhnkite- and Collinsite-Type Compounds Na2me2+(Xo4)2 · 2 h2O (x = S, Me = Mn, CD; and x = Se, Me = Mn, Co, Ni, Zn, CD) and K2Co(Seo4)2 · 2 H2O. *Zeitschrift für Kristallographie - Crystalline Materials* **2003**, *218* (3), 201–209. DOI:10.1524/zkri.218.3.201.20751.